Climate changes of the twentieth through twenty-first centuries simulated by the MRI-CGCM2.3

Seiji Yukimoto, Akira Noda, Takao Uchiyama, Shoji Kusunoki, and Akio Kitoh

Meteorological Research Institute, Tsukuba, Japan

Submitted to Papers in Meteorology and Geophysics

28 April, 2005 (submitted)
12 September, 2005 (revised, 1st)
7 October, 2005 (revised, 2nd)
24 October, 2005 (final form)

Corresponding author: Seiji Yukimoto, Meteorological Research Institute, Nagamine 1-1, Tsukuba, Ibaraki, 305-0052, Japan. E-mail: Yukimoto@mri-jma.go.jp

Abstract

Experiments related to twentieth century historical climate changes and the twenty-first century scenario are performed with the latest version of the MRI climate model, MRI-CGCM2.3. The model reproduces globally averaged surface air temperature (SAT) variations in the twentieth century with satisfactory agreement with interdecadal changes of the observed trend, as well as with the overall SAT increase of 0.5°C at the present-day compared to the pre-industrial level. The globally averaged SAT rises 2.4°C in the late twenty-first century in the experiment for scenario A1B of the Special Report on Emissions Scenarios (SRES) by the Intergovernmental Panel on Climate Change (IPCC). The spatial structures of the simulated trends for the late twentieth century are validated in various atmospheric fields through comparisons with observed data, which indicate that the model demonstrates reasonable agreement with the observed trend in each field. Most of the simulated changes for the twenty-first century reveal spatial patterns similar to those in the trends that appeared in the late twentieth century. The simulated trend patterns of the sea-level pressure (SLP) in both hemispheres bear a resemblance to the observed trends, with each spatial structure reminiscent of the annular modes in the northern and southern hemispheres (NAM and SAM). These SLP trend patterns are consistent with the trends in the SAT, precipitation, and zonal mean zonal wind fields, as in the NAM and SAM. The coherent trend structures of these fields are projected to be enhanced in twenty-first century climate changes. Changes of ocean and sea-ice in association with these atmospheric changes are also described.

1. Introduction

Climate models have become advanced and sophisticated in recent years, and many simulations have been performed with these climate models to project future climate changes. Assessments of future climate changes were made in the Third Assessment Report (TAR) of the Intergovernmental Panel on Climate Change (IPCC, 2001) based upon simulation results from

state-of-the-art climate models (e.g., Johns et al., 2001; Dai et al., 2001). The Meteorological Research Institute (MRI) also contributed to the TAR with results from a climate model newly developed at that time, MRI-CGCM2.0 (Yukimoto et al., 2001). MRI-CGCM2.0 has been updated and released as MRI-CGCM2.3 (Yukimoto et al., 2005); its performance has been improved in many aspects. The model exhibits excellent reproducibility in the present-day climate; the meridional distributions of the radiation budget and cloud radiative forcing are close to the satellite observations (Yukimoto et al., 2005), the seasonal migrations of the Asian monsoon are realistic (Rajendran et al., 2004), and the El Niño-La Niña asymmetry is realistically simulated (An et al., 2005). We used this model to perform experiments to reproduce the historical climate and to project future climate changes. The results are available to the public for use in detailed analyses by many researchers to contribute to the 4th Assessment Report of IPCC (IPCC-AR4). A portion of the experiment results provided lower boundary data for time-slice global warming experiments (Kusunoki et al., 2005; Oouchi et al., 2005) using a very high-resolution atmospheric climate model (Mizuta et al., 2005), with which changes of typhoons, mesoscale phenomena, and extreme events associated with global warming are studied. We describe here the results of a preliminary analysis of climate changes as fundamental information for these studies.

Evaluating how the climate model reproduces twentieth century climate enables us to assess the reliability of the model in projecting future climate changes for the twenty-first century. There are many kinds of known historical external forcing that affect the climate system, such as variations of anthropogenic greenhouse gases and sulfate aerosols, in addition to natural source forcings from solar activity and radiative forcing by volcanic eruptions with stratospheric aerosols. These known natural and anthropogenic external forcing agents are imposed on the climate model in a historical climate simulation, and the simulated climate changes in the twentieth century are compared with the observations. There are only a few instrumental observations that cover the global domain and a long temporal period to detect climate changes in response to such forcings. However, only observations of surface air temperature (SAT; e.g., Jones et al., 1999) and sea-level

pressure (SLP; e.g., Trenberth and Paolino, 1980) have provided relatively comprehensive coverage in the past centuries, particularly in the northern hemisphere (NH). These observations can be used to examine how the climate model reproduces historical climate changes. Validating the simulated variations in the last 30 years of the twentieth century, a period with relatively high observation densities in various atmospheric fields, enables us to examine how climate trends in the twentieth century may be indicative of potential climate changes in the twenty-first century.

The Arctic Oscillation (AO) and the Antarctic Oscillation (AAO), also referred to as the Northern Annular Mode (NAM) and the Southern Annular Mode (SAM), are known to be the dominant variabilities in the extratropical atmospheric circulation (Thompson and Wallace, 2000; Limpasuvan and Hartmann, 1999) that accompany a mass displacement between the polar region and surrounding midlatitudes. Indices of these modes have exhibited a remarkable increasing trend (deepening of the polar low pressure) (e.g., Thompson et al., 2000; Marshall, 2003) in the past few decades, resulting in a significant influence on climate changes in the twentieth century. Thompson et al. (2000) suggested that a large part of the climate trends in the last 30 years of the twentieth century can be accounted for by components congruent with the AO trend.

It is a matter of controversy that whether these observed changes in the atmospheric general circulation are caused by external forcings (particularly by anthropogenic forcing, such as an increase in greenhouse gas concentrations) or the internal variability, and how the modes will change in the future climate. Some of the models simulated changes toward a positive phase of the AO (e.g., Shindell et al., 1999; Fyfe et al., 1999) and AAO (e.g., Cai et al., 2003) in an experiment with a doubled carbon dioxide concentration and in a scenario experiment, though there is presently no consensus regarding historical variations or future changes. Historical experiments with MRI-CGCM2.3 indicated that the response to external forcing exhibits an interdecadal variation that has a SLP pattern similar to the AO (Yukimoto and Kodera, 2005). We investigated the overall climate changes to demonstrate how this variation influences changes in the surface temperature and other climate fields. We also performed scenario experiments to suggest how it will evolve in

the twenty-first century.

This paper is constructed as follows. Section 2 gives a brief description of the model, and Section 3 describes the experiment design. Section 4 reveals the results of the historical experiments and scenario experiments. A summary and discussion are provided in Section 5.

2. Model

We used the latest version of the MRI climate model in this study, referred to as MRI-CGCM2.3. The model has been improved over an early version of the model (MRI-CGCM2.0; Yukimoto et al., 2001), primarily in terms of its cloud scheme and other physical parameterizations, while retaining the fundamental framework. A detailed description of the model and the model's performance in the control climate are given in Yukimoto et al. (2005). The atmospheric component has a horizontal T42 resolution (approximately 280 km transform grid) and 30 layers in the vertical direction, with the top at 0.4 hPa. Longwave radiation is calculated by a multi-parameter random model formulated by Shibata and Aoki (1989), which explicitly addresses absorption by methane (CH_4) and nitrous oxide (N_2O) in addition to water vapor (H_2O), carbon dioxide (CO_2), and ozone (O_3). A delta-two-stream approximation method by Shibata and Uchiyama (1992) is used for the solar radiation calculation. Scattering of solar radiation by atmospheric aerosols (the direct effect) is treated explicitly. Cloud water content is not a prognostic variable but a diagnostic variable dependent on the grid-scale temperature and humidity. The optical properties (single-scattering albedo and asymmetry parameter) are set as constant for all the clouds. Therefore, the indirect effects of atmospheric aerosols (influences of aerosols on cloud properties) are not expressed in the present model. Penetrative convection is parameterized with an Arakawa-Schubert scheme based on a prognostic mass flux formulated by Randall and Pan (1993).

The model treats clouds with a diagnostic cloud scheme based on functions of relative humidity. The vertical profile of critical relative humidity to form clouds was modified from the previous version, which enabled the model to simulate distribution of the radiation budgets close to

the observation. This results in satisfactory performances, such as for the implied ocean meridional heat transport and distributions of the precipitation. The model yields 2.9K for the climate sensitivity (equilibrium response of the global averaged SAT to a doubled CO_2 concentration), which is approximately twice that in the former version. This is primarily attributable to the response of low-level clouds to surface warming with a CO_2 increase (Yukimoto et al., 2005).

The oceanic component is a Bryan-Cox-type global ocean general circulation model (OGCM). The horizontal resolution is 2.5 degrees in longitude and 2.0 degrees in latitude poleward of 12°S and 12°N, with finer resolution up to 0.5 degrees near the equator. The 23 vertical levels are unevenly placed between the surface and the deepest bottom at 5000m, which forms a realistic topography. The sea-ice model calculates compactness and thickness prognostically based on thermodynamics and horizontal advection and diffusion. The advection velocities are determined from the surface ocean current multiplied by an empirical constant (set to one-third in our experiments).

We used flux corrections for the experiments. The improvements in the latest version of the model enable it to reproduce a reasonably realistic climate without using flux corrections. However, we believe it is more important to simulate basic states for climate changes as close to the actual present-day conditions as possible, since the results will be used in studies on a regional scale.

3. Experiments

The experiments analyzed in this paper include a pre-industrial control experiment (PIcntrl), a historical climate experiment for the twentieth century (20C3M), and three SRES (IPCC, 2000) scenario experiments for the twenty-first century. The abbreviations follow the convention for the IPCC AR4. The forcing agents of the experiments and the configurations of individual experiments (as summarized in Table 1) are described below.

a. Forcing Agents

The external forcing in our experiments consists of four categories of agents, which are greenhouse gas concentrations, tropospheric sulfate aerosol, solar irradiance, and radiative forcing due to volcanic stratospheric aerosols.

The greenhouse gases include three species, CO_2, CH_4, and N_2O, which were imposed by specifying them as well-mixed concentrations. Forcing due to chlorofluorocarbons (CFCs), which are not explicitly treated in the model's radiation scheme, were imposed as additional CO_2 concentrations with equivalent radiative forcing. Note that the ozone concentration change was not included in the forcing in our experiments; we could not obtain any appropriate ozone distribution data that was consistent between the historical experiment and the scenario experiments.

Tropospheric sulfate aerosol forcing was imposed only for the direct effect (scattering of solar radiation by aerosol droplets). The indirect effect of sulfate aerosol is known to significantly impact surface temperature changes. However, the indirect effect was not included in the experiments because it was difficult to treat it appropriately with the present model. We included aerosol loading from both natural and anthropogenic sources. The column total sulfate aerosol from natural sources was estimated as a residual from the total and anthropogenic sulfate mass distributions (the data is available at http://gacp.giss.nasa.gov/transport/) derived by the GACP transport model by Tegen et al. (1997). The distribution of the natural source sulfate aerosol reveals a greater amount over the tropical oceans because of marine biogenic dimethylsulfide (DMS) emission.

The solar activity forcing was simply imposed by changing the solar constant, and the spectral change associated with the solar activity was not included. The reconstructed historical record of the total solar irradiance is based on Lean et al. (1995; updated data are available at http://www.giss.nasa.gov/data/simodel/solar.irradiance/). The reconstruction data includes an 11-year activity cycle and a longer-term component based on sunspot variations.

The effect of stratospheric aerosols due to volcanic activity was introduced by reducing the solar irradiance at the model's top of the atmosphere (by changing the solar constant) as a

substitution. The "direct" response in the lower stratosphere to volcanic forcing differs from that to solar forcing with equivalent radiative forcing for the troposphere and ocean (e.g., Shindell et al., 2001). However, volcanic forcing has a relatively short time scale (a couple of years at most), so we believe the substitution does not greatly affect the present results since we are focusing on long-term climate changes. The volcanic radiative forcing F was estimated by a simple formula for solar constant change ΔS_0 as $F = \Delta S_0 (1-\alpha)/4$, where α is the reference planetary albedo (=0.31). We specified $\Delta S_0 = -60\tau$ in the 20C3M experiment, where τ is the optical thickness of the volcanic aerosols estimated by Sato et al. (1993; data are available at http://www.giss.nasa.gov/data/strataer/). The radiative forcing is accordingly expressed as $F = -10.4\tau$. This is less than the estimation $F = -23.5\tau$ by Sato et al. (1993).

b. Pre-industrial Control Experiment

The Pre-industrial control experiment (PIcntrl) simulates an unperturbed climate state with anthropogenic forcings at the pre-industrial level and is used as the reference for the following historical and scenario experiments. PIcntrl also provides the initial states for the 20C3M simulations. The initial state of the simulation was taken from the final state of the 450-year pre-industrial spin-up (PIspup) integration, which initiated from the end of the present-day spin-up integration (428-year length, see Yukimoto et al., 2005). PIspup was integrated with a fully coupled mode and was long enough that there was little climatic drift, at least in the upper ocean. The length of the PIcntrl simulation is 750 years (the data for the first 350 years were provided for the IPCC-AR4).

The forcing agents for the PIspup and PIcntrl simulations were fixed at the levels of year 1850, i.e., CO_2 = 290 ppmv, CH_4 = 792 ppbv, N_2O = 285 ppbv, CFCs = 0, and solar constant = 1366.0 Wm^{-2}, and the sulfate aerosol was from natural sources only. The aerosol mass was given in the column total and was vertically distributed with a homogeneous mixing ratio in the lower 740 m thickness of the atmosphere. Volcanic forcing was not included.

c. Historical Experiment (20C3M)

Historical experiment 20C3M simulates climate changes in the twentieth century by imposing known historical records of external forcing. The 20C3M results are evaluated to assess how the model reproduces past climate changes and to provide the initial states for the SRES scenario experiments. The 20C3M experiment consisted of five member ensemble simulations. Using their ensemble average can eliminate dependence on the initial conditions and the internal variability. The initial states of each member simulation were taken from the different states of the PIcntrl simulation at years 1, 51, 101, 151, and 201. Each simulation encompassed 151 years, from 1850 through 2000.

The forcing agents of the experiment included the historical records of (or estimated) greenhouse gases (CO_2, CH_4, N_2O and CFCs), tropospheric sulfate aerosol, volcanoes, and solar forcing. Temporal changes of each greenhouse gas concentration were specified by the data after Hansen et al. (1998; data are available from http://www.giss.nasa.gov/data/simodel/ghgases/). The total mixing ratios of the CFCs were converted to equivalent CO_2 and added to the CO_2 concentration. The radiative forcing by the total halocarbons was scaled as 0.3 Wm^{-2} at the 1990 level and included as 21 ppmv of the equivalent CO_2. The column total tropospheric sulfate mass loading was specified with a geographical distribution and vertically distributed with a homogeneous mixing ratio in the lower 740 m thickness of the atmosphere. The variation of sulfate mass loading were expressed by multiplying the geographical patterns for 1986 and 2050 (Figs. 1a and 1b of Mitchell and Johns, 1997) by the time-series of weight obtained by linear interpolation from the decadal-means given in Mitchell and Johns (1997). The forcing variations by solar and volcanic activities were imposed as the solar constant variation, as described in the previous section.

d. Scenario Experiments

The scenario experiments simulate climate changes in the twenty-first century, imposing future

anthropogenic forcings based on the SRES marker scenario (IPCC, 2000). We used A1B, A2, and B1 scenarios (abbreviated experiment names are SRESA1B, SRESA2, and SRESB1) in this study. Each experiment consisted of five member ensemble simulations. Each member simulation started from the state of year 1990 in the 20C3M simulations, although the 20C3M simulations were extended until year 2000. The simulations cover years 1990 through 2100 (111-year length).

Temporal concentration changes for CO_2, CH_4, and N_2O were specified for each marker scenario. The concentration data were provided by IPCC (2001, Appendix II.2), based on the ISAM-model. The CFC concentration changes were not included. Three-dimensional distributions of sulfate aerosol for the SRES experiments were derived by the MRI chemical transport model (MASINGAR; Tanaka et al., 2003) for every ten years in each scenario. The temporal change of global total sulfate mass loading (unit: Tg) for each SRES marker scenario is provided in Fig. 1. No solar or volcanic forcing was included in the SRES experiments, so the solar constant was fixed at 1367 Wm^{-2}.

4. Results

a. Radiative Forcing

Temporal variations of globally averaged net radiative forcing at the tropopause for the 20C3M and SRES experiments are illustrated in Fig. 2. The radiative forcing includes the effect of stratospheric adjustment since it was calculated with 15-month period off-line integrations, with all the states except radiative heating held fixed by those of the reference run (the present-day control simulation; Yukimoto et al., 2005). Each the off-line integration started from the same state in the reference run, but with the forcing of every year for the 20C3M experiment and decadal intervals for the SRES experiments. All external forcings for each experiment were included in the calculation.

The radiative forcing increased approximately 1.5 Wm^{-2} at the end of the twentieth century

from the pre-industrial level. The increase rate is greater in the last 30 years of the twentieth century than in the preceding period, due to a rapid increase of anthropogenic greenhouse gases. There are a number of pulses with negative forcing due to major volcanic eruptions with a maximum magnitude of 1 Wm^{-2}. There is an active period in the late nineteenth century that includes the eruptions of Krakatau (1883, Indonesia) and several successive volcanoes revealed as depressions of the radiative forcing. This is followed by a relatively calm period until the 1963 eruption of Agung (Indonesia), with outstanding pulses also due to the eruptions of El Chichon (Mexico) in 1982 and Pinatubo (Philippine) in 1991. However, the magnitude of these radiative forcing changes related to volcanoes is roughly one third of the estimation by Sato et al. (1993), as was previously suggested.

SRESA2 exhibits the largest increase of forcing in the scenario experiments, exceeding 4 Wm^{-2} in the late twenty-first century. SRESA1B exhibits a more rapid increase than SRESA2 in the earlier half of the century followed by a moderate increase, and reaches 3.4 Wm^{-2} at the end of the century. The forcing in SRESB1 exhibits the least increase and almost no increase in the late twenty-first century, reaching 2.2 Wm^{-2}.

b. Surface Air Temperature

The globally averaged annual mean SAT simulated in each experiment is presented in Fig. 3, together with that from the observation. The ensemble means and ensemble scatters are displayed. The values are plotted as deviations from the reference climate of the 1961 to 1990 average. The observational data for comparison was taken from HadCRUT2v (Jones and Moberg, 2003), which is based on air temperature over land (with the variance adjusted for the effects of changes in station number) combined with the sea surface temperature (SST; HadISST; Rayner et al., 2003) over the oceans. It is reported that the anomalies over the oceans agree well between the night marine air temperature and SST (Jones and Moberg, 2003).

The increase of the simulated SAT in the 1961 to 1990 average was 0.5 °C, relative to the pre-industrial level. This value agrees with the observed SAT change for the same period. The rate

of increase in the 1970s through the 1990s reveals good agreement with the observation, which exists within the simulated ensemble scatter. The detailed fluctuation also appears to agree for the instantaneous perturbations related to the outstanding volcanic events in 1982 and 1991, showing coincidence between the ensembles and the observation. There appears to be a small discrepancy with the observed volcanic signal, at least in the globally averaged SAT variation, although the volcanic forcing may be underestimated. The simulated temperature decrease in response to the Agung eruption (in 1963) is not distinct compared with other major volcanic events. There is a decade around the 1880s with a significant temperature depression that is consistent among the ensembles and can be attributed to several volcanic forcings, including the Krakatau eruption in 1883. However, no significant signal can be found for the observed temperature, which may be related to uncertainty in the magnitude of the volcanic forcing or an insufficiency of the SAT observation density. The observed warming around 1940 is underestimated in the simulation, and the observed negative trend in the 1940s through 1960s is not clearly reproduced.

The increase rates of the SAT in the early twenty-first century are similar in the scenario experiments, but reveal differences throughout the middle to late century that corresponds to the different forcing scenarios. SRESA2 produces the greatest warming in the late twenty-first century, with an increase of over 3°C at the end of the century, and a suppressed increase in the latter half for SRESA1B that leads to about a 0.5°C lower increase. The SRESB1 experiment exhibits the least increase throughout the twenty-first century. The SAT changes were averaged for the target 20-year period of 2080 to 2099 and are presented in Table 2. The averaged temperature increases for SRESA1B, SRESA2, and SRESB1 are 2.4, 2.7 and 1.7°C.

Linear trends of the globally averaged annual mean SAT changes were estimated for each experiment and the observations for the selected 30-year periods of interest; they are depicted in Fig. 4. The same grid masking of missing data in the observation was applied to the 20C3M experiment to evenly compare the anomalies between the simulated and observed global averages. Only grid points with 12-month observations for the year were used to obtain the global average; the grid

points were otherwise masked out. The observed temperature anomaly is not based on the air temperature but on the SST, and thus the temperature anomaly over the sea-ice region may be largely different from the SST anomaly in winter. Therefore, comparing the observation with the simulated SAT may not be appropriate over the sea-ice region. However, we confirmed that most sea-ice regions are excluded by the masking and that the influences of including the sea-ice region are very small, even if they are calculated with all the available data covering some part of the sea-ice regions.

The observed trends reveal an increase trend of 0.14 (±0.05) K/decade in 1911 to 1940, a weak decrease trend of –0.02 (±0.04) K/decade in 1941 to 1970, and a large increase trend of 0.19(±0.05) K/decade in the last 30 years of the twentieth century. The magnitude of the positive trend of 0.17 (±0.04) K/decade in 1971 to 2000 in the 20C3M experiment is close to the observed value. The reliability of the observed trend in the recent period is greater than in other periods due to the high observation density. Furthermore, the increase rate of greenhouse gases became remarkable and their forcing became predominant over other obscure forcings. Therefore, the agreement of the SAT trend in this period supports the model's reliability to simulate climate changes due to anthropogenic forcing.

The observation exhibits a relatively large increase trend in the period of 1911 to 1940, regardless of there being no significant change in radiative forcing. This trend is underestimated in the 20C3M experiment. The discrepancy can be attributed to the combination of volcanic effect and solar effect. The cooling effects (suppression of warming) of successive volcanic activities in the 1880s were sustained for several decades. However, those effects ended coincidently in the period of rapid increase of solar activity from the 1920s through 1940s, which could have led to greater warming. The model underestimates the interdecadal variation of the ocean heat uptake compared to that observed (Levitus et al., 2001), which probably resulted in reducing the timescale of response to volcanic cooling effect. In contrast, solar activity variations have only very small radiative forcing (about 0.2 Wm^{-2} for the difference between the 1910s and 1940s), but there are

distinct variations in its spectral distribution, which affects stratospheric circulation changes through interactions with the stratospheric ozone. However, these processes were not incorporated in the simulations because the ozone concentration was prescribed and solar activity was imposed only by solar constant variations (no spectral variations).

The model does not sufficiently reproduce the observed SAT negative trend in the period of 1941 to 1970. The simulated trend is close to zero although it exists within the error bar for the observation. The increase of sulfate aerosol in this period was substantial, whereas the increase rate of greenhouse gases was relatively moderate. The model does not include the indirect effect of aerosols, which possibly leads to underestimation of the negative radiative forcing of sulfate aerosol. Another reason for the disagreement may be the interdecadal internal variation. The observed interdecadal variation may not be a response to external forcing but a manifestation of the internal variability of the climate system. We speculate that the simulated internal variability may have been smaller than the actual one.

SRESA1B indicates a change in the trends from 0.28 (±0.02) K/decade in 2041 to 2070 to 0.16 (±0.02) K/decade in the last 30 years of the twenty-first century, whereas SRESA2 suggests considerable (0.35-0.36 K/decade) positive trends with similar magnitudes throughout the century.

The geographical distributions of the annual-mean SAT trends were examined for the 30-year periods of 1971 to 2000 for the late twentieth century trends and 2071 to 2100 for the late twenty-first century trends, as indicated in Fig. 5. The observed trend was calculated only for the grid points at which the annual mean anomalies were available for more than 50% of the period. The observed late twentieth century trend indicates substantial positive trends over the continents in middle-eastern Eurasia and northern North America. A basin scale pattern is seen in the Pacific with suppressed warming or slight cooling in the midlatitude North Pacific and relatively significant warming in the central-eastern tropical Pacific, which resembles the dominant interdecadal variability in the Pacific known as the Pacific decadal oscillation (PDO; Mantua, 1997). The 20C3M ensemble (Fig. 5b) also exhibits a significant warming trend over the Eurasian

continent, though it shifts north-westward compared with the observation, and the trend over North America is less than that observed. There are large positive trends in the marginal sea-ice regions in the Arctic Ocean, which are associated with decreases of sea-ice coverage and thickness as described later. However, these warming trends cannot be compared with the observations due to a lack of data coverage. A weak cooling trend is simulated in the Labrador Sea and at the southern edge of Greenland. No cooling trend is obvious in the observation for the annual mean trend; however, the observed trend for winter (not shown) exhibits a significant negative trend in that region. The SRESA2 ensemble (which indicates the greatest global warming among the scenarios) reveals a large-scale geographical pattern similar to that of 20C3M but with globally larger positive values, and the warming trends are very intense in the marginal sea-ice region in the Arctic Ocean. The El Niño-like pattern in the tropical Pacific is prominent, though it is not apparent in the 20C3M ensemble. The relatively substantial warming trends over land in the Sahara through the Middle East, South Africa, and Australia become significant and also share regional features with the observed twentieth century trends.

Similarities of the geographical patterns of SAT trend are examined with the spatial correlations for the late twentieth century (1971 to 2000) trends of the observation and 20C3M and for the mid-twenty-first century trends (2041 to 2070) of the SRES experiments (Table 3). We used a weighting by the square root of the cosine of the latitude in the calculation so that the covariance would be normalized by the area for each grid box. The simulated twentieth century trend in the 20C3M ensemble has a low spatial correlation (0.11) with the observed trend. Both the SAT trends of the model experiment (in each ensemble member) and the observation are considered to contain internal long-term (longer than interdecadal) variability as well as a response to external forcing. It is difficult to separate the internal variability from the observed trend, while it is possible for the ensemble experiment to obtain the response to external forcing (Fig. 5b) by taking the ensemble mean and separating the internal variability. The SAT trend pattern that appears in one of the ensemble members (run-4, Fig. 5c) displays a broad geographical resemblance to the observed trend

pattern (Fig. 5a), particularly in the Pacific. The trend pattern that results from subtracting the ensemble mean from the total variation of this member (Fig. 5d) can be regarded as the long-term component (with the same timescale as expressed in the observed trend) of the internal variability in the model. This pattern exhibits a PDO-like feature in the Pacific with a negative anomaly in the central-eastern North Pacific and a positive anomaly in its southeastern side that extends to the eastern tropical Pacific. The dominant interdecadal variability in the experiment without external forcing (PIcntrl, figure not shown) also has a similar large-scale pattern. This internal variability pattern has a spatial correlation of 0.24 with the observed trend, while the trend pattern for the combined internal variability and response to external forcing of run-4 (Fig. 5c) has a correlation of 0.31 with the observed trend. We infer from this relationship that a sizable part of the observed trend pattern may be internal variability. The simulated trend patterns exhibit relatively high spatial correlations. 20C3M reveals correlations of 0.69 with SRESA1B and 0.64 with SRESA2, suggesting evidence that a large part of the ensemble twentieth century trend is a manifestation of the response to anthropogenic forcing. SRESB1 reveals a somewhat different response. This may be related to its overall small climate change trend, leading to relatively large internal variability.

Seasonal differences of the SAT change in the SRES experiments were examined for 20-year averages for 2080 to 2099. Figure 6 depicts the geographical distribution of the SAT changes for the December to January (DJF) mean and June to August (JJA) mean. Both seasons reveal similar features in the low latitudes that are also similar to the annual-mean trend pattern. In contrast, the warming is substantial in winter and minimal in summer in the high latitudes. The model simulates very strong warming in winter, particularly in the marginal sea-ice regions where the sea-ice significantly decreases (Spitsbergen through Novaya Zemlya and the Chukchi Sea in the Arctic Ocean, the Sea of Okhotsk, and the Antarctic Ocean).

We examined the spatial correlations of the seasonal (DJF and JJA) changes averaged for 2080 to 2090 in the SRES experiments (Table 4) to evaluate how future changes in the seasonal fields resemble the trends of the corresponding seasonal fields simulated for the late twentieth century.

The correlations for changes in each field were calculated against the trends in the corresponding seasonal ensemble mean field simulated in the 20C3M for the period of 1971 to 2000. The spatial correlations for the observed trend for 1971 to 2000 are also presented for comparison. The spatial patterns of the SAT changes exhibit correlations of 0.55 to 0.67 with the late twentieth century trends. The correlations are greater in boreal winter (DJF) than in summer (JJA) for all the scenarios. The correlation with the observed trend is much less than that of simulated future changes, though it is greater in DJF (0.14) than in JJA (0.06). The individual geographical patterns of the averaged SAT changes in the SRES experiments reveal few differences (the spatial correlations were greater than 0.98), and they are also similar to the result from a transient climate response (TCR) experiment reported by Yukimoto et al. (2005). The spatial differences in the changes are also small for variables other than the SAT; therefore, we will hereafter describe the changes only in results from SRESA1B.

c. Precipitation

The globally averaged precipitation consistently increased in correspondence to the simulated global warming. The changes averaged for 2080 to 2099 indicate increases of 5.4% for the SRESA1B ensemble, 5.7% for the SRESA2 ensemble, and 3.7% for the SRESB1 ensemble relative to the 1961 to 1990 average in the 20C3M ensemble (Table 2). Figure 7 depicts the geographical distributions of the precipitation change rate in the SRESA1B ensemble averaged for 2080 to 2099 relative to the 1961 to 1990 average in the 20C3M ensemble. The large-scale patterns for precipitation changes are also close to the results from the TCR experiment, as well as the SAT. Precipitation increases in the high latitudes for both seasons (DJF and JJA), but with a greater increase rate in winter in both hemispheres. There are remarkable decreases around the Mediterranean and in Central Asia, and a large percentage increase in the arid region of the southern part of Arabia through Pakistan in the northern summer. The notable increase in the central-eastern equatorial Pacific is associated with an El-Niño-like surface-temperature change

(Fig. 6). Spatial correlations with the simulated twentieth century trends are also examined for the precipitation change rate (Table 4). The correlations are 0.22 to 0.31 in DJF and 0.44 to 0.50 in JJA. All the experiments indicate greater geographical similarity in northern summer (JJA) than in winter (DJF). We consider that there would be greater uncertainty in projecting future precipitation changes from the observed twentieth century trend than from the SAT changes due to the more sizable internal variability. However, the correlations among the SRES experiments (not shown) are considerable (over 0.96), which implies a robust structure in the anthropogenic climate change signal.

d. Sea Level Pressure

The observed and simulated late twentieth century (1971 to 2000) trends of the northern hemisphere (NH) sea-level pressure (SLP) are presented in Fig. 8. We used HadSLP1 (an update of GMSLP2; Basnett and Parker, 1997) for the SLP observation data. The simulated trend for the 20C3M ensemble exhibits an annular pattern with a negative trend in the Arctic and a positive trend in the surrounding midlatitude band, and its broad feature resembles the AO pattern. The model can simulate a realistic month-to-month AO (Yukimoto and Kodera, 2005) with one action center (center of anomaly) around Iceland and the other action center with the opposite sign anomaly in the midlatitude eastern North Atlantic near the Azores anticyclone center. The pattern in the late twentieth century trend reveals several features different from the short-term AO pattern. One of the action centers around Iceland is displaced toward the North Pole, and the action center over the eastern Atlantic is shifted eastward and extends to the Mediterranean through central Asia. These features are consistent with the observed trend, although the observed trend displays a somewhat different pattern in the North Pacific. The hemispheric pattern of the NH winter SLP change in the SRESA1B ensemble (2080 to 2099 average, Fig. 9) is similar to the late twentieth century trends with a spatial correlation of 0.63, except that the positive anomaly in the Mediterranean shifts further eastward and the negative anomaly in the Arctic becomes stronger around the Bering Strait.

Figure 10 presents the time-series of covariance between the NH winter (DJF) mean SLP anomaly fields in the SRES ensembles and the simulated SLP trend pattern in the late twentieth century (Fig. 8b). This temporal variation suggests how the trend pattern has emerged as a dominant response to anthropogenic forcing and how it is detectable in the historical SLP variation. It also demonstrates how it will evolve in the future climate. The temporal variations indicate a continuous increase from the 1970s through the twenty-first century, suggesting that the trend pattern that emerged in the late twentieth century is embedded in the climate change signal in the twenty-first century. A temporal variation for the observed SLP trend pattern obtained by a similar calculation is also plotted in Fig. 10. The values are multiplied by a factor based on the standard deviation ratio for the period of 1871 to 1970 relative to that of the 20C3M ensemble (since the magnitude of the variation becomes very small when the ensemble is made into a mean). The observed variation also indicates a distinct increase since the 1970s, which is consistent with the fact that the AO index has exhibited a significant increasing trend in the recent 30-year period in the twentieth century (Thompson et al., 2000). These agreements between the simulated and observed trends in the late twentieth century imply that the response of the extratropical atmosphere to the anthropogenic greenhouse gas forcing has a spatial structure similar to the AO. One reasonable explanation for the AO-like response is as follows. The polar vortex is enhanced by stratospheric cooling due to the increase of greenhouse gases, which leads to a tropospheric AO-like circulation pattern through a wave-mean flow interaction (Shindell et al., 2001). However, it must be noted that the observed SLP trend may contain a sizable AO-like internal variability with an interdecadal timescale (Yukimoto and Kodera, 2005), as previously discussed for the SAT trend. The variations generally indicate an increasing tendency in the twenty-first century for all the SRES scenarios, though there are large interdecadal variations (even when we average five member ensembles) comparable to differences among the scenarios. It is difficult to distinguish the response difference that corresponds to the difference in forcing among the scenarios. This suggests that the climate change signal is not robust in the NH SLP due to the considerable internal variability.

The SLP trend in the southern hemisphere (SH) reveals an annular pattern similar to the observed SAM (Fig. 11). Examinations of each season (not shown) indicated that the pattern is dominant throughout the year, while the annular pattern trend in the NH is dominant only in winter. This may be related to the climatological characteristics in the SH, where the polar vortex lasts much longer and the SAM is observed in all seasons (Hartmann and Lo, 1998). Temporal variations regressed onto the trend pattern (Fig. 12) also indicates a significant increasing trend throughout the twentieth and twenty-first centuries for all the scenarios. The interdecadal variability appears smaller than in the NH, which enables us to recognize differences among the scenarios in response to each forcing. It has been suggested that the observed SAM trend (e.g., Marshall, 2003; Renwick, 2004) is influenced by ozone depletion in the lower stratosphere (Thompson et al., 2000). However, the ozone change was not included in the forcing agents in our experiments, which suggests that the annular pattern trend in the climate change can emerge even without the ozone change. The response would likely become stronger if the ozone depletion was accounted for as a forcing.

e. Atmospheric Zonal-mean Fields

Figure 13 depicts the meridional vertical structure of the late twentieth century trends in the zonal-mean zonal wind for the DJF mean in the simulation and in the ECMWF reanalysis (ERA-40; Simmons and Gibson, 2000). The simulated trend reveals a westerly anomaly in the NH polar stratosphere that extends down to the troposphere. This corresponds to an intensification of the polar vortex, which shares a feature with the NAM. The trend in ERA-40 indicates a weak westerly anomaly around 60°N in the troposphere and the lower stratosphere, which partly agrees with the simulated trend, but there is no signal of intensified vertical shear in the stratosphere. However, the statistical confidence level is low in the stratospheric trend of the reanalysis since there is substantial interannual variability and the observation period is short. In contrast, the results from the 20C3M experiment reveal greater confidence with reduced internal variability since the ensemble average is made. The simulation exhibits a notable increasing westerly trend around 60°S

in the SH that grows vertically from the surface to the stratosphere, accompanying an easterly trend at 40°S to comprise a meridional dipole structure. This feature is similar to the SAM and also agrees well with the observed trend. This simulated SAM-like trend is outstanding in the southern summer (DJF). Thompson et al. (2000) suggested that the positive trend of the SAM is most marked in November, and they associated it with the ozone losses in spring. Our result indicates seasonality similar to the observed trend, although our experiment did not include the ozone change. In addition, an easterly trend is simulated in the tropical upper troposphere, which seems consistent with the reanalysis data. The similarity of the overall structure of the trend was evaluated by obtaining a spatial correlation (mass weighted); the value between the reanalysis and 20C3M was 0.52 (Table 4).

A trend structure in the zonal-mean air temperature (Fig. 14) is simulated with the typical features of a warming in the troposphere and a cooling in the stratosphere. This structure is a well-known response to the increase of greenhouse gases and is obviously different from that in the internal variability (Yukimoto and Kodera, 2005). This structure also agrees with the observational trend in the broad-scale features. The simulated trend indicates strong cooling in the polar stratosphere in accordance with the intensification of the polar vortex (Fig. 13b), though it does not appear in the reanalysis (which has below 95% statistical significance in that region). Strong cooling (95% significance) is observed in the Arctic lower stratosphere, which can be associated with the effect of ozone depletion, although the model does not indicate this signal.

The change in the zonal wind in the late twenty-first century (Fig. 15a) is similar to that of the late twentieth century trend (Fig. 13b) in many features (spatial correlation 0.79, Table 4). However, the axis of the westerly anomaly in the winter NH in the twenty-first century change inclines toward the low latitudes in the lower stratosphere. The change accompanies the upward and equator-ward shift with some intensification of the subtropical jets in both hemispheres. This may be related to the uplift of the tropopause; a detailed analysis will be required to interpret the change. The extratropical SH reveals the same structure as in the twentieth century trend. The zonal-mean

temperature structure (Fig. 15b) reveals good agreement (spatial correlation 0.98, Table 4) with the simulated late twentieth century trend. There is a significant warming at about 4 K in the tropical upper troposphere that exceeded 6 K in the northern high latitudes near the surface.

f. Ocean

Ocean Temperature

We examined the ocean temperature change in the SRESA1B experiment for the zonal average (Fig. 16). The ocean is evenly warmed by approximately 0.3°C at a 1000 m depth, except for the high latitudes. A deep intrusion of the warming at 60°N is attributable to deep overturning of the Atlantic Ocean. In contrast, the warming in the interior Arctic Ocean is confined as shallow due to the strong stability in that region.

Thermohaline Circulation

The maximum Atlantic overturning (Fig. 17) indicates a decline with time, from 19 Sv in the early twentieth century to less than 18 Sv in the late twenty-first century in the SRESA1B and SRESA2 experiments. A different magnitude of weakening in the twenty-first century among the scenarios appears to approximately correspond to the magnitude of surface warming. These weakenings can be explained by a strengthening of the upper ocean stability in the sinking region, as a result of freshening by the precipitation increase in the North Atlantic, as indicated in Fig. 7, in addition to surface heating.

Sea-level Change

Sea-level change is an important consequence of climate change and significantly impacts society and the environment. Global-mean sea-level changes are related to several factors, including the thermal expansion of seawater and freshwater inflow from land water (melting of glaciers and ice sheets). We examined only the effects of thermal expansion and the local height anomaly

change since the present model does not represent variations of glaciers or ice sheets. The thermal expansion is directly linked to the ocean heat uptake. Levitus et al. (2001) estimated it as 18.2×10^{22} J for the period between the 1950s and 1990s, based on the linear trend of the ocean temperature. Our 20C3M experiment yields a similar value of 15×10^{22} J for the same period. The globally averaged sea-level was elevated 12.2 cm by thermal expansion in the late twenty-first century in the SRESA1B experiment. This value is smaller than the results from other models (IPCC, 2001) by about 1/2 to 1/4, which implies that our model may underestimate the future ocean heat uptake. Local sea-surface height anomalies are caused by ocean circulation changes. The geographical distribution of the local height change (Fig. 18) indicates a relatively greater anomaly in the North Pacific with a maximum of 20 cm east of Japan, which is associated with the AO-like atmospheric circulation change (as discussed later). There are also zonally elongated regions of notable anomalies around 40°S in the Southern Ocean and relatively lesser anomalies around Antarctica, which are probably associated with a SAM-like atmospheric circulation change.

g. Sea-ice

The sea-ice significantly decreases in both its coverage and thickness in correspondence to the surface warming. The geographical distributions of the sea-ice compactness changes are depicted in Fig. 19. The sea-ice retreats in the marginal sea-ice regions in both seasons of maximum and minimum extent. The retreat is more prominent in summer since the ice-albedo feedback enhances the change. However, its impact on the atmosphere is much less than in winter, since the temperature difference between the sea-ice surface and the sea-ice free area is minimal in summer.

The total area and volume in the NH and SH for each experiment are provided in Table 5. The maximum total sea-ice area (March) in the NH decreases 14% from 13.5×10^{12} m^2 (20C3M; 1961 to 1990) to 11.6×10^{12} m^2 (SRESA1B; 2080 to 2099), and the minimum area (September) decreases 37% from 7.6×10^{12} m^2 to 4.8×10^{12} m^2. The reduction ratio of the winter area is minimal in the SH, and the total area in September decreases 7% from 17.6×10^{12} m^2 to 16.3×10^{12} m^2. However, the

total area reduction is significant (–59%) in summer (March). The sea-ice thickness markedly decreases in accordance with the warming over all the sea-ice regions, not only in the marginal regions (the distribution is not shown). The total volume of the sea ice in the NH decreases 56% from 38.1×10^{12} m^3 to 16.8×10^{12} m^3 in winter (March). The thickness reduction in winter significantly impacts the surface temperature, since the heat conduction in the sea ice increases substantially if the thickness is considerably reduced.

5. Summary and Discussion

Experiments related to twentieth century historical climate changes and a twenty-first century scenario were performed with the latest version of the MRI climate model, MRI-CGCM2.3, which has been improved in terms of reproducing the present-day climate (Yukimoto et al., 2005). Ensemble simulations were carried out in the historical experiment by imposing the anthropogenic forcing from greenhouse gases of CO_2, CH_4, N_2O, and CFCs and the direct effect of tropospheric sulfate aerosol, as well as the natural source forcing from solar activity and the radiative effect of volcanic stratospheric aerosols, for the period from the mid-nineteenth century to the end of the twentieth century. The changes of greenhouse gas concentrations and tropospheric sulfate aerosol in the twenty-first century were imposed in the scenario experiments based on the IPCC SRES (IPCC, 2000).

The model reproduces the globally averaged SAT variation in the twentieth century with good agreement in the interdecadal changes of its trends. The simulated temperature rise during the late twentieth century (the average of 1961 to 1990) from the pre-industrial level is 0.5°C, which agrees with the observed value. The simulated SAT trend in the last 30 years exhibits very good agreement with the observed trend, which suggests the reliability of the model in projecting future climate changes. The globally averaged SAT in the scenario experiments rise 2.4°C for SRESA1B, 2.7°C for SRESA2, and 1.7°C for SRESB1 in the late twenty-first century (the average of 2080 to 2099).

The geographical distribution of the SAT change simulated for the twenty-first century reveals

several features that have been present in many previous modeling studies. The geographical trend pattern of the NH winter SAT in the late twentieth century reveals a broad pattern similar to that seen in the model's realistic AO (Yukimoto and Kodera, 2005). The trend pattern indicates a significant warming trend in the region of northern Eurasia extending to Japan and a slight cooling around the Labrador Sea. This warming pattern is expected to enhance in the twenty-first century, overlying the globally averaged temperature rise. The experiments suggest a regional feature with related minimal warming around the Labrador Sea in the North Atlantic for the twenty-first century simulations, which has been commonly seen in most model results for future climate projections (IPCC 1996, 2001). This feature has been explained to be a result of substantial ocean heat uptake associated with deep overturning of the North Atlantic (e.g., Manabe et al., 1991). The AO-like atmospheric circulation change probably contributes to the anomaly pattern in addition to the oceanic effect.

The simulated SLP trend pattern in the late twentieth century also agrees with the observed pattern. The NH winter SLP decreases in the Arctic region but increases in the surrounding midlatitude band, representing an annular pattern that shares some features with the AO. However, unlike the AO, the simulated pattern does not have an action center near Iceland, and the center of the positive anomaly in the Atlantic shifts toward the Mediterranean. The SH SLP trend reveals a year-round pattern close to the SAM pattern. The experiments suggest that the annular patterns in both hemispheres that appeared in the late twentieth century would develop along with the climate change during the twenty-first century. However, the climate change signal in the NH is relatively small since its internal variability is considerable.

The model reproduces an intensification of the westerly wind in the extratropical troposphere, extending to the stratosphere with an equivalent barotropic vertical structure. This feature is found in the winter season in the NH and almost year-round for the SH. The structures are reminiscent of the NAM in the NH and SAM in the SH, and are projected onto the twenty-first century change. An upward and equator-ward shift of the subtropical jets in both hemispheres is also simulated when

the global warming becomes significant in the twenty-first century, though it is not apparent in the twentieth century trend. The result is consistent with Kushner et al. (2001) in that the SH extratropical response is strongly projected onto the SAM simulated in their model, and also there are westerly wind anomalies in the tropical upper troposphere.

The present experiments suggest that the zonally averaged temperature change is apparently not related with the NAM and SAM, although the wind field response implies that the structure is projected onto those dominant variabilities. The temperature response reveals features familiar in previous studies (e.g., Mitchell et al., 1990; Rind et al., 1998), i.e., a warming in the troposphere with a maximum in the tropical upper troposphere associated with the warmer moist adiabatic vertical profile and a cooling in the stratosphere associated with enhanced radiative cooling by increased greenhouse gases.

The precipitation in the simulated twenty-first century climate increases in both summer and winter seasons at high latitudes with a greater increase rate in winter. The AO-like atmospheric circulation change is reflected on the remarkable precipitation increases in northern Europe. The increase of freshwater flux into the northern North Atlantic, in conjunction with the ocean surface warming, leads to stronger ocean vertical stability and possibly contributes to weakening of the Atlantic overturning.

The sea-level changes in the twenty-first century were estimated from the effects of thermal expansion of seawater and ocean circulation changes. A greater elevation is projected in the midlatitude northwestern Pacific with a maximum east of Japan. This regional sea-level change is attributable to a northward shift and enhancement of the North Pacific subtropical gyre. The Sverdrup streamfunction anomaly (not shown), calculated from the ocean surface wind stress change, agreed well with the sea-level change anomaly (Sato et al., 2005). This implies that the anticyclonic anomaly over the midlatitude North Pacific, as a part of the AO-like change (Fig. 9), contributes to ocean circulation changes.

We evaluated many aspects of the historical climate changes simulated by the model and

found that the model produces changes consistent with the observed trends in the twentieth century. These results support the reliability of using the model to project twenty-first century climate changes. More detailed analyses using the results of these model experiments are left for future study.

Acknowledgements

The authors are grateful to K. Kodera and Y. Kuroda for their valuable comments and discussions. This work was funded by the Climate Change Prediction Fund (Study of the Prediction of Regional Climate Changes over Japan due to Global Warming) under the Japan Meteorological Agency, and the Global Environment Research Fund and the Global Environment Research Coordination System under Ministry of the Environment. The computations were performed on NEC SX-6 supercomputers at the Meteorological Research Institute and at the Center for Global Environmental Research, the National Institute for Environmental Studies.

References

An, S.-I., and Y.-G. Ham, J.-S. Kug, F.-F. Jin, and I.-S. Kang, 2005: El Niño-La Niña asymmetry in the Coupled Model Intercomparison Project simulations. *J. Climate*, **18**, 2617-2627.

Basnett, T. and D. Parker, 1997: Development of the Global Mean Sea Level Pressure Data Set GMSLP2, Climate Research Technical Note, 79, Hadley Centre, Met Office, FitzRoy Rd, Exeter, Devon, EX1 3PB, UK.

Cai, W.J., P.H. Whetton, and D.J. Karoly, 2003: The response of the Antarctic Oscillation to increasing and stabilized atmospheric CO_2. *J. Climate*, **16**, 1525-1538.

Dai, A., T.M.L. Wigley, A. Boville, J.T. Kiehl, and L.E. Buja, 2001: Climates of the twentieth and twenty-first centuries simulated by the NCAR Climate System Model. *J. Climate*, **14**, 485-519.

Fyfe, J.C., G.J. Boer, and G.M. Flato, 1999: The Arctic and Antarctic Oscillations and their projected changes under global warming. *Geophys. Res. Lett.*, **26** 1601-1604.

Hansen, J., M. Sato, A. Lacis, R. Ruedy, I. Tegen, and E. Mathews, 1998: Climate forcings in the industrial era. *Proc. Natl. Acad. Sci. USA*, **95**, 12753-12758.

Hartmann, D.L., and F. Lo, 1998: Wave-driven zonal flow vacillation in the Southern Hemisphere. *J. Atmos. Sci.*, **55**, 1303-1315.

IPCC, 1996: Climate Change 1995: The Science of Climate Change. J.T. Houghton, L.G. Meira Filho, B.A. Callander, N. Harris, A. Kattenberg and K. Maskell (Eds.), Cambridge University Press, UK. pp 572.

IPCC, 2000: Special Report of the Intergovernmental Panel on Climate Change. Nebojsa Nakicenovic and Rob Swart (Eds.), Cambridge University Press, UK. pp 570.

IPCC, 2001: Climate Change 2001: The Scientific Basis, Intergovernmental Panel on Climate Change, Contribution of Working Group I to the Third Assessment Report of the Intergovernmental Panel on Climate Change. (Eds. Houghton, J.T., Y. Ding, D.J. Griggs, M. Noguer, P.J. van der Linden, X. Dai, K. Maskell, and C.A. Johnson), Cambridge University Press, Cambridge, United Kingdom and New York, NY, USA, 881pp.

Johns, T.C., J.M. Gregory, W.J. Ingram, C.E. Johnson, A. Jones, J.A. Lowe, J.F.B. Mitchell, D.L. Roberts, D.M.H. Sexton, D.S. Stevenson, S.F.B. Tett, and M.J. Woodge, 2001: Anthropogenic climate change for 1860 to 2100 simulated with the HadCM3 model under updated emissions scenarios. Hadley Centre Technical Note No. 22, The Hadley Centre for Climate Prediction and Research, The Met Office, London Road, Bracknell, RG12 2SY, UK.

Jones, P.D., and A. Moberg, 2003: Hemispheric and large-scale air temperature variations: An extensive revision and an update to 2001. *J. Climate*, **16**, 206-223.

Jones, P.D., M. New, D.E., Parker, S. Martin, and I.G., Rigor, 1999: Surface air temperature and its variations over the last 150 years. *Reviews of Geophysics*, **37**, 173-199.

Kushner, P.J., I.M. Held, and T.L. Delworth, 2001: Southern Hemisphere atmospheric circulation response to global warming. *J. Climate*, **14**, 2238-2249.

Kusunoki, S., J. Yoshimura, H. Yoshimura, A. Noda, K. Oouchi and R. Mizuta, 2005: Change of Baiu in global

warming projection by an atmospheric general circulation model with 20-km grid size. *submitted to J. Meteor. Soc. Japan*.

Lean J., J. Beer, and R. Bradley, 1995: Reconstruction of solar irradiance since 1610; implications for climate change, *Geophys. Res. Lett.*, **22**, 3195-3198.

Levitus, S., J.I. Antonov, J. Wang, T.L. Delworth, K.W. Dixion, A.J. Broccoli, 2001; Anthropogenic warming of earth's climate system. *Science*, **292**, 267-270.

Limpasuvan, V., and D. Hartmann, 1999: Eddies and the annular modes of climate variability. *Geophys. Res. Lett.*, **26**, 3133-3136.

Manabe, S., R.J. Stouffer, M.J. Spelman, and K. Bryan, 1991: Transient responses of a coupled ocean-atmosphere model to gradual changes of atmospheric CO_2. Part I. Annual mean response. *J. Climate*, **4**, 785–818.

Mantua, N.J. and S.R. Hare, Y. Zhang, J.M. Wallace, and R.C. Francis, 1997: A Pacific interdecadal climate oscillation with impacts on salmon production. *Bull. Amer. Meteor. Soc.*, **78**, 1069-1079.

Marshall, G.J., 2003: Trends in the southern annular mode from observational and reanalyses. *J. Climate*, **16**, 4134.

Mitchell, J.F.B., and T.C. Johns, 1997: On modification of global warming by sulfate aerosols. *J. Climate*, **10**, 245-267.

Mitchell, J., S. Manabe, V. Meleshko, and T. Tokioka, 1990: Equilibrium climate change and its implications for the future. Climate Change. The IPCC Scientific Assessment. J.T. Houghton, G.J. Jenkins, and J. Ephraums (Eds.), Cambridge University Press.

Mizuta, R., K. Oouchi, H. Yoshimura, A. Noda, K. Katayama, S. Yukimoto, M. Hosaka, S. Kusunoki, H. Kawai, and M. Nakagawa, 2005: 20km-mesh global climate simulations using JMA-GSM model. (*submitted to J. Meteor. Soc. Japan*)

Oouchi, K., J. Yoshimura, H. Yoshimura, R. Mizuta, S. Kusunoki and A. Noda, 2005: Tropical cyclone climatology in a global-warming climate as simulated in a 20km-mesh global atmospheric model. (*submitted to J. Meteor. Soc. Japan*)

Parker, D.E., L.V., Alexander, and J. Kennedy, 2004: Global and regional climate in 2003. *Weather*, **59**, 145-152.

Rajendran, K., A. Kitoh, and S. Yukimoto, 2004: South and East Asian monsoon climate and variation in the MRI coupled model (MRI-CGCM2). *J. Climate,* **17**, 763-782.

Randall, D., and D.-M. Pan, 1993: Implementation of the Arakawa-Schubert cumulus parameterization with a prognostic closure. Meteorological Monograph/The representation of cumulus convection in numerical models, 46, 145-150.

Rayner, N.A., D.E. Parker, E.B. Horton, C.K. Folland, L.V. Alexander, D.P. Rowell, E.C. Kent, and A. Kaplan, 2003: Global analyses of sea surface temperature, sea ice, and night marine air temperature since the late nineteenth century, *J. Geophys. Res.*, **108**(D14), 4407, doi:10.1029/2002JD002670.

Renwick, J.A., 2004: Trends in the Southern Hemisphere polar vortex in NCEP and ECMWF reanalyses. *Geophys. Res. Letts.*, **31**, doi:10.1029/2003GL019302.

Rind, D., D. Shindell, P. Lonergan, and N.K. Balachandran, 1998: Climate change and the middle atmosphere. Part III:

The doubled CO2 climate revisited, *J. Climate*, **11**, 876-894.

Sato, M., J.E. Hansen, M.P. McCormick, and J.B. Pollack, 1993: Stratospheric aerosol optical depth, 1850-1990, *J. Geophys. Res.*, **98**, 22987-22994.

Sato, Y., S. Yukimoto, H. Tsujino, H. Ishizaki, and A. Noda, 2005: Response of North Pacific ocean circulation in a Kuroshio-resolving ocean model to an Arctic Oscillation (AO)-like change in Northern Hemisphere atmospheric circulation due to greenhouse-gas forcing. (*submitted to J. Meteor. Soc. Japan*)

Shibata, K. and T. Aoki, 1989: An infrared radiative scheme for the numerical models of weather and climate. *J. Geophys. Res.*, **94**, 14923-14943.

Shibata, K. and A. Uchiyama, 1992: Accuracy of the delta-four-stream approximation in inhomogeneous scattering atmospheres. *J. Meteor. Soc. Japan*, **70**, 1097-1109.

Shindell, D.T., R.L. Miller, G. Schmidt, and L. Pandolfo, 1999: Simulation of recent northern winter climate trends by greenhouse-gas forcing. *Nature*, **399**, 452-455.

Shindell D., G.A. Schmidt, R.L. Miller, D. Rind, 2001: Northern Hemisphere winter climate response to greenhouse gas, ozone, solar, and volcanic forcing. *J. Geophys. Res., D, Atmos.*, **106**, 7193-7210.

Simmons, A.J., and J.K. Gibson, 2000: The ERA-40 Project plan, ERA-40 Proj. Rep. Ser. 1, 63 pp., Eur. Cent. for Medium-Range Weather Forecasts, Reading, UK.

Tanaka, T., K. Orito, T. Sekiyama, K. Shibata, M. Chiba and H. Tanaka, 2003: MASINGAR, a global tropospheric aerosol chemical transport model coupled with MRI/JMA98 GCM: Model description, *Pap. Meteor. Geophys.*, **53**, 119-138.

Tegen, I., P. Hollrig, M. Chin, I. Fung, D. Jacob, and J. Penner 1997: Contribution of different aerosol species to the global aerosol extinction optical thickness: Estimates from model results. *J. Geophys. Res.* **102**, 23895-23915.

Thompson D.W.J. and J.M. Wallace, 2000: Annular modes in the extratropical circulation. Part I: Month-to-month variability. *J. Climate*, **13**, 1000-1016.

Thompson, D.W.J., J.M. Wallace, G.C. Hegerl, 2000: Annular modes in the extratropical circulation. Part II: Trends. *J. Climate*, **13**, 1018-1036.

Trenberth, K.E., D.A. Paolino Jr., 1980: The Northern Hemisphere sea-level pressure data set: trends, errors and discontinuities. *Mon. Wea. Rev.*, **108**, 855–872.

Yukimoto, S. and K. Kodera, 2005: Interdecadal Arctic Oscillation in twentieth century climate simulations viewed as internal variability and response to external forcing, *Geophys. Res. Lett.*, **32**, L03707.

Yukimoto. S., A. Noda, A. Kitoh, M. Hosaka, H. Yoshimura, T. Uchiyama, K. Shibata, O. Arakawa, and S. Kusunoki, 2005: Present-day climate and climate sensitivity in the Meteorological Research Institute Coupled GCM, version 2.3 (MRI-CGCM2.3). (*submitted to J. Meteor. Soc. Japan*)

Yukimoto, S., A. Noda, A. Kitoh, M. Sugi, Y. Kitamura, M. Hosaka, K. Shibata, S. Maeda, and T. Uchiyama, 2001: The new Meteorological Research Institute coupled GCM (MRI-CGCM2). – Model climate and variability –. *Pap. Meteor. Geophys.*, **51**, 47-88.

Tables

Table 1. Configurations of the experiments

Experiment	Period (year)	Ensemble Number	Greenhouse Gas Concentrations				Sulfate Aerosol (direct effect)	Solar Forcing (solar constant, Wm^{-2})	Volcano Activity
			CO_2 (ppmv)	CH_4 (ppbv)	N_2O (ppbv)	CFCs (equiv. CO_2)			
PIcntrl	1851-2600	1	290	792	285	0	natural (GACP)	1366	0
20C3M	1851-2000	5	Hansen et al. (1998)				natural + anthrop. (GACP)	Lean et al. (1995)	Sato et al. (1993)
SRESA1B	1990-2100	5	IPCC (2001) SRES A1B			0	natural (GACP) + anthrop. (SRES A1B)	1367	0
SRESA2	1990-2100	5	IPCC (2001) SRES A2			0	natural (GACP) + anthrop. (SRES A2)	1367	0
SRESB1	1990-2100	5	IPCC (2001) SRES B1			0	natural (GACP) + anthrop. (SRES B1)	1367	0

Table 2. Temporal averages for surface air temperature and precipitation simulated in each experiment and changes from the reference climate (1961 to 1990 averages in the 20C3M).

Experiment	Average Period (years)	SAT (Change) [°C]	Precipitation [mm/day] (Change)
20C3M	1961-1990	13.03	2.553
SRES-A1B	2080-2099	15.42 (2.39)	2.690 (5.4%)
SRES-A2	2080-2099	15.76 (2.73)	2.699 (5.7%)
SRES-B1	2080-2099	14.73 (1.70)	2.648 (3.7%)

Table 3. Spatial correlations among the trend patterns of the annual mean SAT for the observation (HadCRUT2v), 20C3M, and SRES experiments.

	20C3M	SRESA1B	SRESA2	SRESB1
HadCRUT2v	0.11	0.21	0.31	0.26
20C3M	-	0.69	0.64	0.33
SRESA1B	-	-	0.82	0.51
SRESA2	-	-	-	0.65

Table 4. Spatial correlations of the observed trends (1971 to 2000) and the simulated changes (SRES experiments, averages for 2080 to 2099) for the various fields with the simulated late twentieth century trends (by 20C3M for 1971 to 2000) for the corresponding fields

	Observations	SRES-A1B	SRES-A2	SRES-B1
SAT change (DJF)	0.14	0.67	0.67	0.64
SAT change (JJA)	0.06	0.60	0.55	0.61
Precipitation change rate (DJF)	0.00	0.31	0.31	0.22
Precipitation change rate (JJA)	–0.26	0.50	0.44	0.50
NH sea-level pressure change (DJF)	0.57	0.63	0.50	–0.09
SH sea-level pressure change (annual)	0.46	0.92	0.91	0.88
Zonal mean zonal wind change (DJF)	0.52	0.79	0.83	0.81
Zonal mean zonal wind change (JJA)	0.14	0.94	0.93	0.93
Zonal mean air temperature change (DJF)	0.46	0.98	0.98	0.97
Zonal mean air temperature change (JJA)	0.41	0.99	0.99	0.99

Table 5. Total area and volume in the NH and SH in March and September for each experiment

	Area [10^{12} m^2]				Volume [10^{12} m^3]			
	NH		SH		NH		SH	
Experiment	Mar.	Sep.	Mar.	Sep.	Mar.	Sep.	Mar.	Sep.
20C3M	13.5	7.6	3.5	17.6	38.1	29.2	1.9	11.8
SRESA1B	11.6	4.8	1.4	16.3	16.8	9.0	0.4	8.8
SRESA2	11.5	4.8	1.4	16.3	16.5	8.9	0.4	8.8
SRESB1	12.1	5.3	2.1	16.6	20.2	12.1	0.9	10.0

Figure Captions

Fig. 1. Temporal change of global total sulfate mass loading (unit: Tg) imposed for SRESA1B (thick solid), SRESA2 (dashed line) and SRESB1 (thin solid) experiments.

Fig. 2. Temporal variations of the global averaged net (longwave + shortwave) radiative forcing at the tropopause with stratospheric adjustments for the 20C3M (thin solid line) and SRES (A1B: thick solid line, A2: dashed line, and B1: dotted lines) experiments.

Fig. 3. Temporal variations of the globally averaged annual mean SAT for the PIcntrl (grey), 20C3M (blue) and SRES (A1B: red, A2: orange, and B1: green) experiments and the observation (black). The ensemble means are plotted in lines and the ensemble scatters (ranges between the maximum and minimum) are plotted with shadings. The ensemble mean for the PIcntrl was calculated from the five 250-year time-series sampled from the single simulation with a lag every 50 years.

Fig. 4. Linear trends of the globally averaged annual mean SAT for the 20C3M (blue) and SRES (A1B: red, A2: orange, and B1: green) experiments and the observation (black) for the selected five 30-year periods (1911 to 1940, 1941 to 1970, 1971 to 2000 for historical periods and 2041 to 2070 and 2071 to 2100 for the future periods). Error bars denote 95% confidence limits estimated from the interannual variance in each period.

Fig. 5. Geographical distributions of linear trends of the annual mean SAT for the (a) observation, (b) 20C3M (ensemble mean), (c) 20C3M (run-4) and (d) 20C3M (internal variability in the run-4) for the period 1971 to 2000, and (e) SRESA2 for the period 2071 to 2100. The unit is K/decade. Regions lacking data coverage (less than 50% of the period) are stippled.

Fig. 6. Geographical distributions of the simulated SAT change in the SRESA1B ensemble averaged for 2080 to 2099 for the (a) DJF mean and (b) JJA mean.

Fig. 7. Geographical distributions of the simulated precipitation change rate (%) in the SRESA1B ensemble averaged for 2080 to 2099 for the (a) DJF mean and (b) JJA mean.

Fig. 8. Geographical distribution of linear trends of the DJF mean NH sea-level pressure for the

(a) observation (in hPa decade^{-1}) and (b) 20C3M ensemble (in hPa (30-yr)$^{-1}$) for the period 1971 to 2000.

Fig. 9. Geographical distribution of the NH (DJF mean) sea-level pressure change in the SRESA1B ensemble (2080 to 2099 average, in hPa) relative to the 20C3M ensemble (1961 to 1990 average).

Fig. 10. Temporal variations of the NH (DJF mean) SLP change in the SRES ensembles for 1850 to 2100 (including the preceding 20C3M) regressed onto the simulated trend pattern for 1971 to 2000. A low-pass filter with a 20-year period was applied after the regression. A similar regression for 1871 to 2000 is plotted for the observed SLP (HadSLP1) variation with a dashed-and-dotted curve.

Fig. 11. Same as in Fig. 9, except for the SH annual mean SLP.

Fig. 12. Same as in Fig. 10, except for the SH annual mean SLP.

Fig. 13. Meridional vertical structure of the linear trends in the zonal-mean zonal wind (DJF mean) for the (a) observation (ERA-40, unit is m s^{-1} decade^{-1}) and (b) 20C3M ensemble (unit is m s^{-1} (30 yr)$^{-1}$ for the period 1971 to 2000.

Fig. 14. Same as Fig. 13, except for the zonal-mean air temperature (DJF-mean). Units are (a) K decade^{-1} and (b) K (30 yr)$^{-1}$.

Fig. 15. Meridional vertical structure of the zonal-mean changes in the SRESA1B ensemble (average for 2080 to 2099) relative to the 20C3M ensemble (average for 1961 to 1990) for the DJF-mean (a) zonal wind (ms^{-1}) and (b) air temperature (K).

Fig. 16. Zonally averaged annual-mean ocean potential temperature change (K) for the SRESA1B ensemble (average for 2080 to 2099) relative to the 20C3M ensemble (average for 1961 to 1990).

Fig. 17. Temporal variation of the maximum annual Atlantic overturning (Sv) with the 5-year moving average for the PIcntrl, 20C3M, and SRES ensembles. The maximum values were searched for each monthly mean, and their annual and ensemble means were then calculated. The ensemble

mean for PIcntrl was calculated from the five 250-year time-series sampled from the single simulation with lags every 50 years.

Fig. 18. Sea-surface height change (cm) including the global sea-level change in the SRESA1B ensemble (average for 2080 to 2099) relative to the 20C3M ensemble (average for 1961 to 1990).

Fig. 19. Mean sea-ice coverage change (fraction) in the SRESA1B ensemble (average for 2080 to 2099) relative to the reference climate (1961 to 1990 average in the 20C3M ensemble) for the (a) NH in March, (b) NH in September, (c) SH in March, and (d) SH in September. The purple dashed lines denote regions of reference climate.

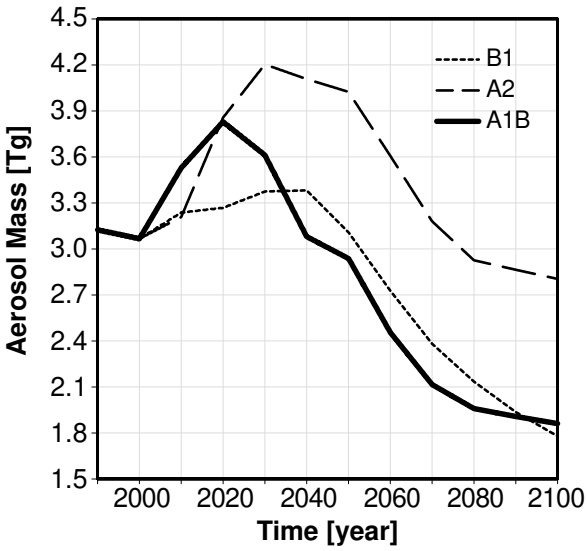
4.5
4.2
3.9
3.6
3.3
3.0
2.7
2.4
2.1
1.8
1.5
Aerosol Mass [Tg]
2000
2020
2040
2060
2080
2100
Time [year]
B1
A2
A1B

Figure 1

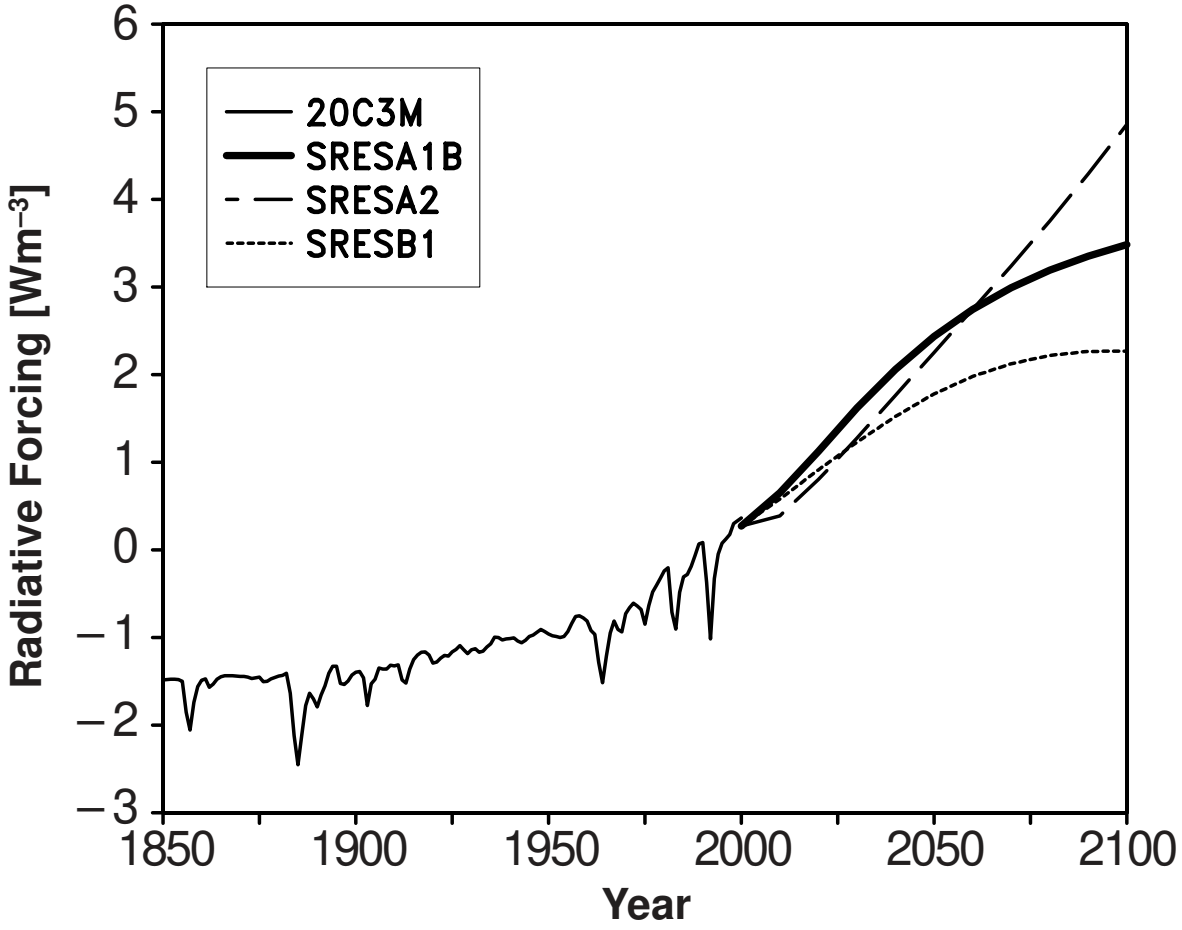
20C3M
SRESA1B
SRESA2
SRESB1
Radiative Forcing [Wm^{-3}]
Year
6
5
4
3
2
1
0
−1
−2
−3
1850
1900
1950
2000
2050
2100

Figure 2

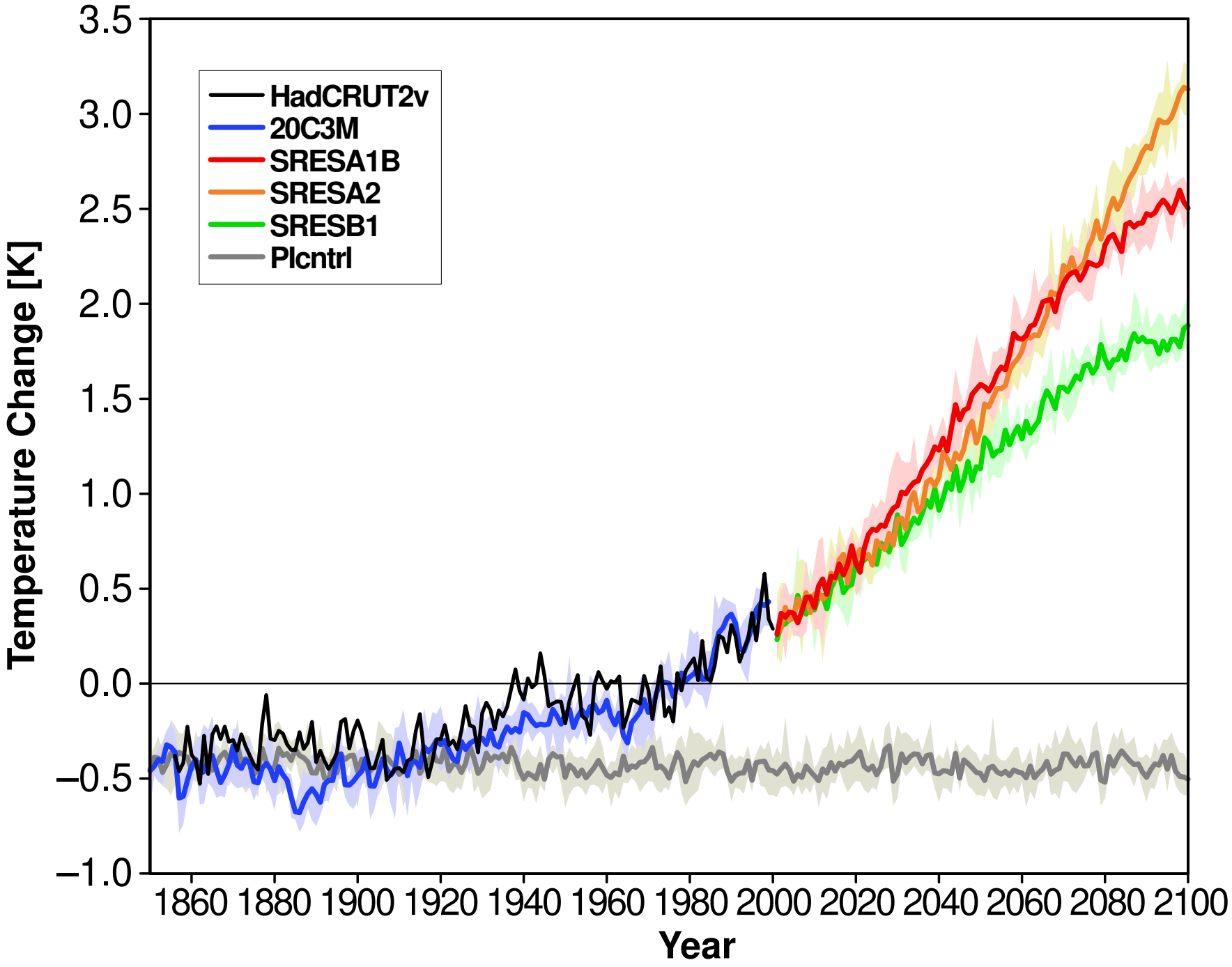
HadCRUT2v
20C3M
SRESA1B
SRESA2
SRESB1
Plcntrl
Temperature Change [K]
3.5
3.0
2.5
2.0
1.5
1.0
0.5
0.0
−0.5
−1.0
1860 1880 1900 1920 1940 1960 1980 2000 2020 2040 2060 2080 2100
Year

Figure 3

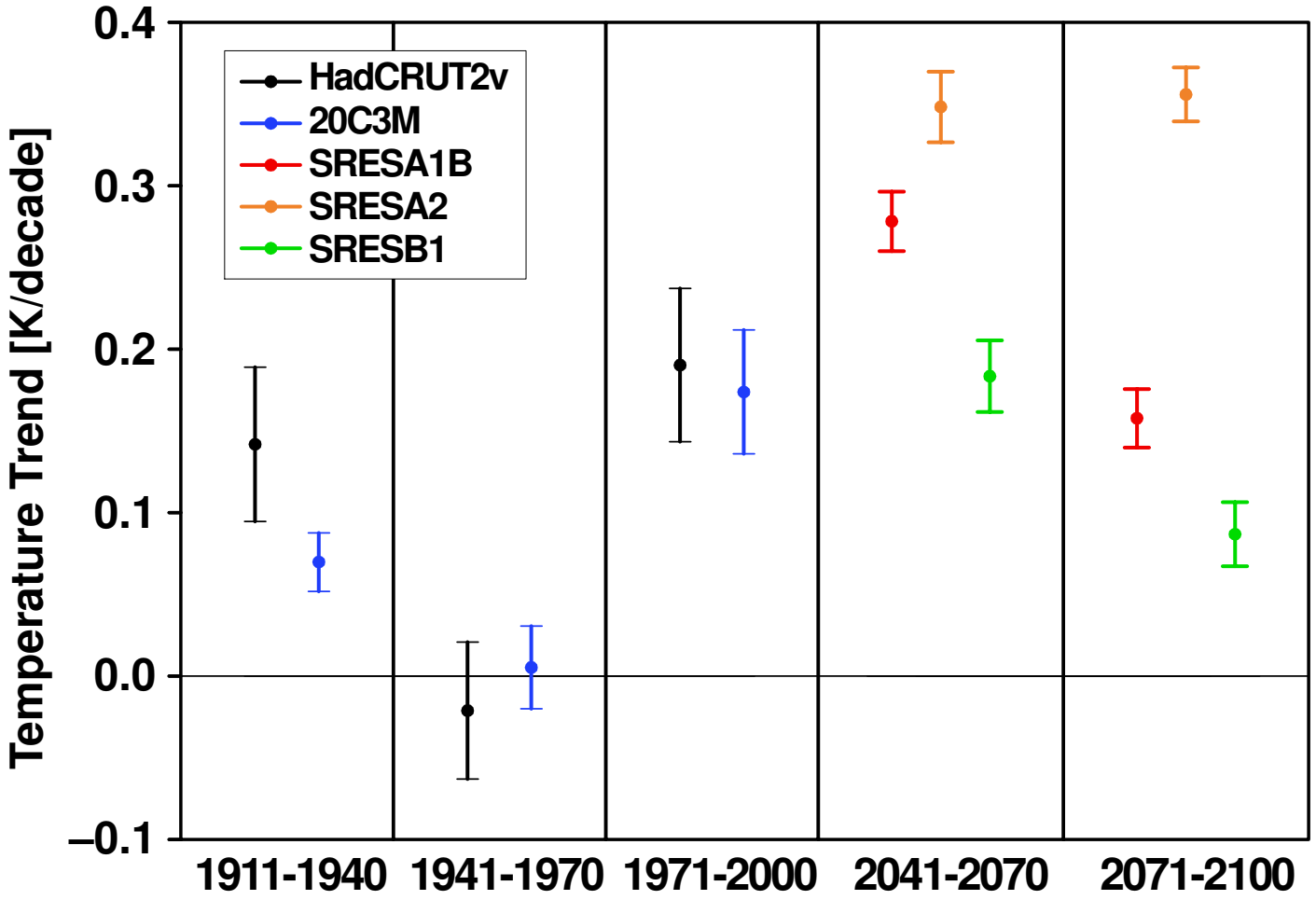
0.4
0.3
0.2
0.1
0.0
–0.1
Temperature Trend [K/decade]
HadCRUT2v
20C3M
SRESA1B
SRESA2
SRESB1
1911-1940
1941-1970
1971-2000
2041-2070
2071-2100

Figure 4

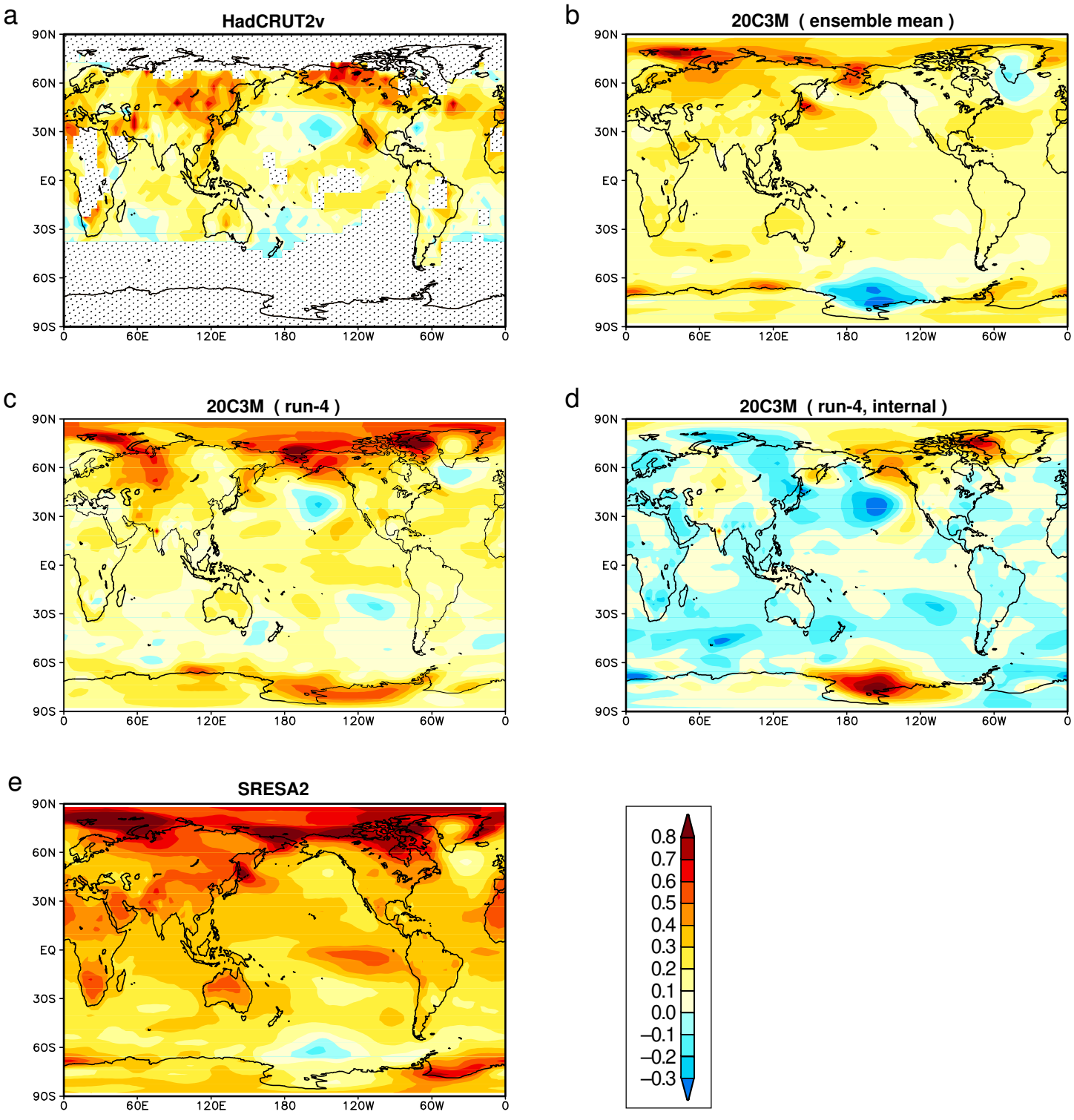
a
HadCRUT2v
b
20C3M (ensemble mean)
c
20C3M (run-4)
d
20C3M (run-4, internal)
e
SRESA2
90N
60N
30N
EQ
30S
60S
90S
0
60E
120E
180
120W
60W
0.8
0.7
0.6
0.5
0.4
0.3
0.2
0.1
0.0
−0.1
−0.2
−0.3

Figure 5

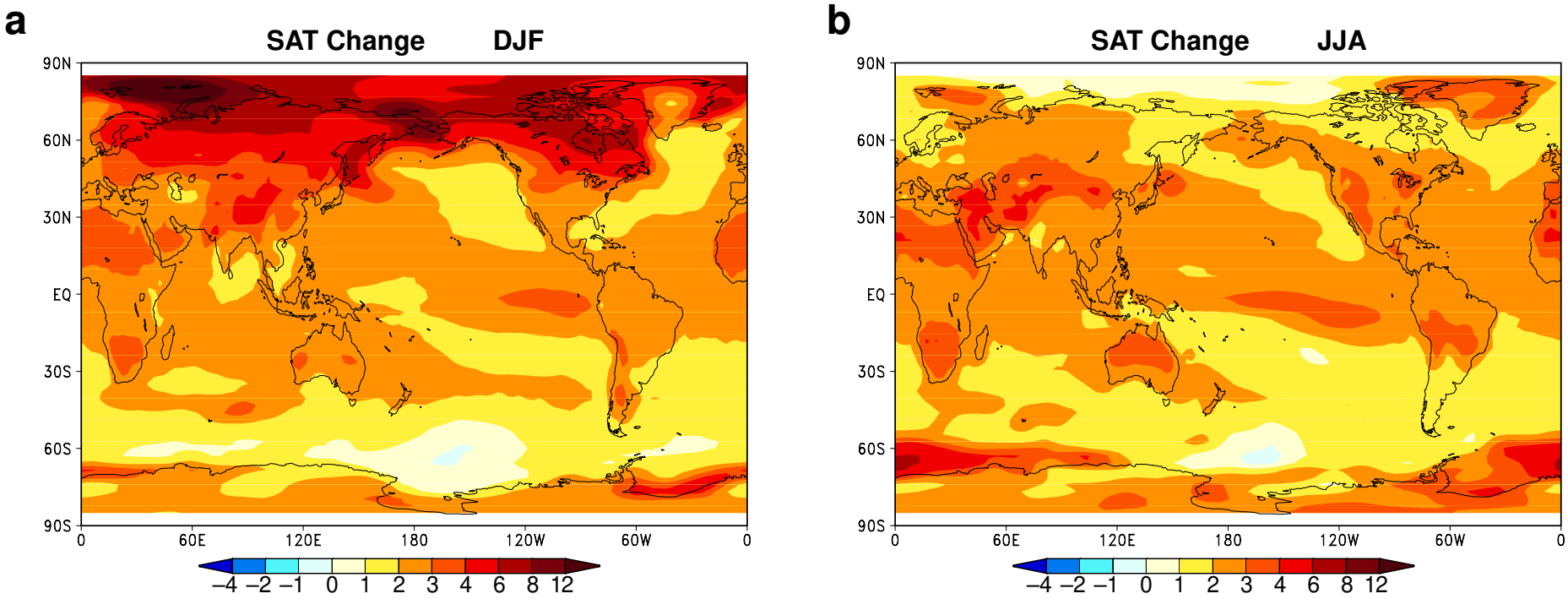
a
SAT Change DJF
90N
60N
30N
EQ
30S
60S
90S
0
60E
120E
180
120W
60W
0
−4 −2 −1 0 1 2 3 4 6 8 12
b
SAT Change JJA
90N
60N
30N
EQ
30S
60S
90S
0
60E
120E
180
120W
60W
0
−4 −2 −1 0 1 2 3 4 6 8 12

Figure 6

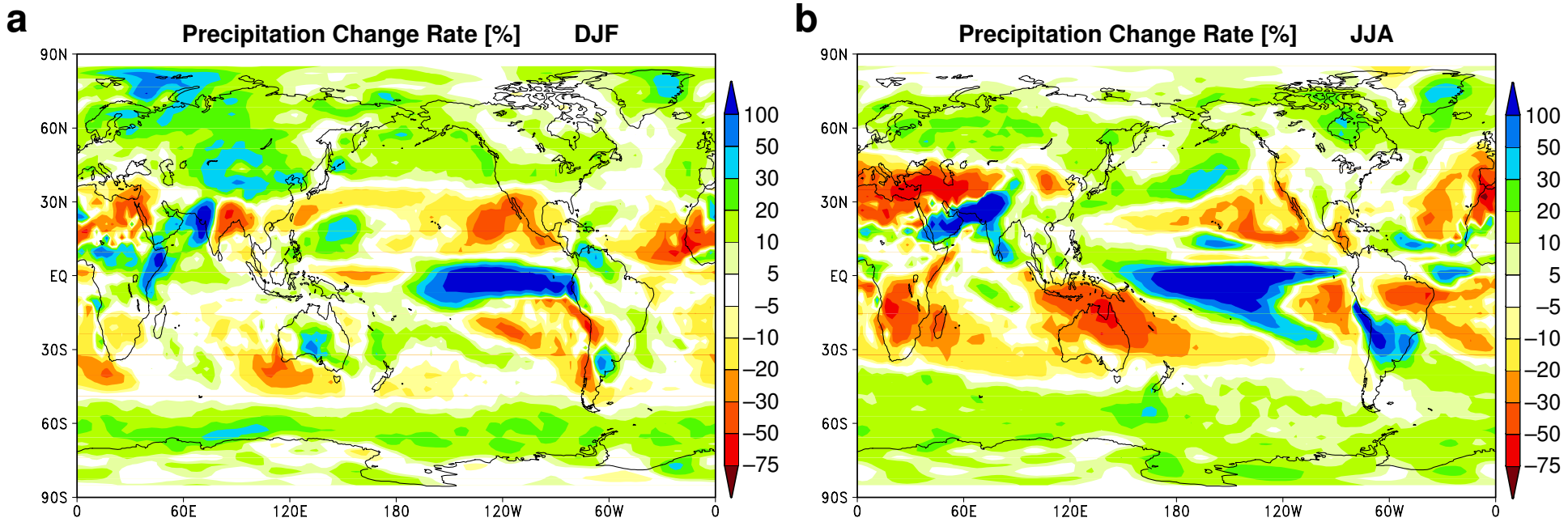
a
Precipitation Change Rate [%] DJF
90N
60N
30N
EQ
30S
60S
90S
0
60E
120E
180
120W
60W
0
100
50
30
20
10
5
−5
−10
−20
−30
−50
−75
b
Precipitation Change Rate [%] JJA
90N
60N
30N
EQ
30S
60S
90S
0
60E
120E
180
120W
60W
0
100
50
30
20
10
5
−5
−10
−20
−30
−50
−75

Figure 7

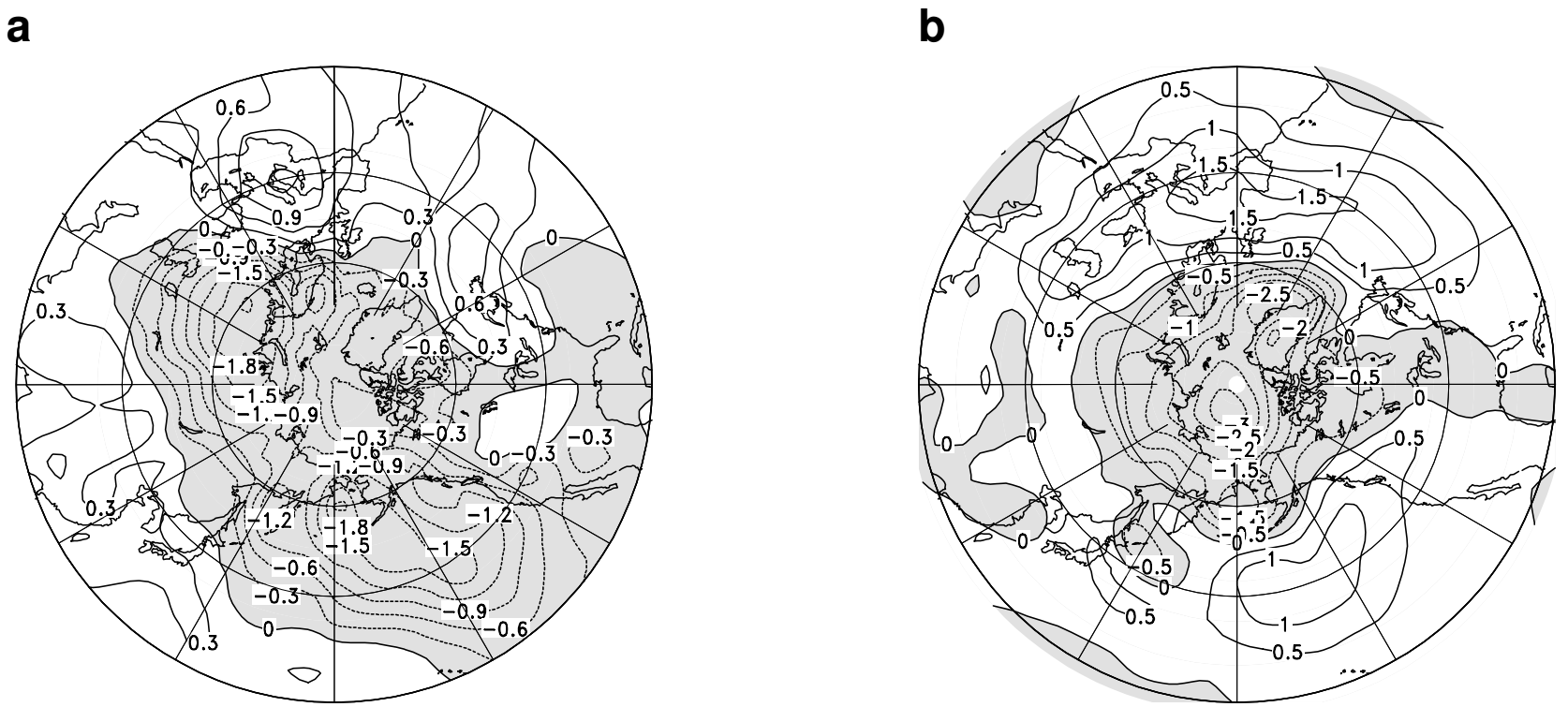

Figure 8

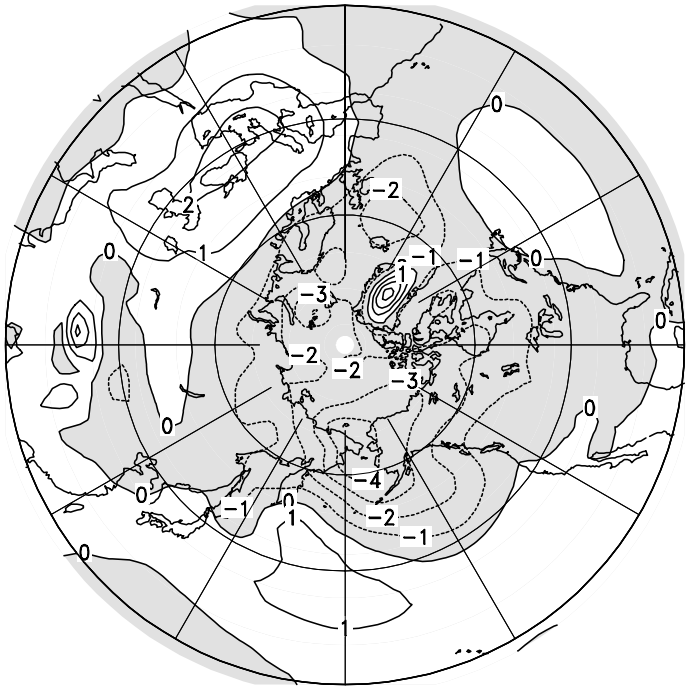

Figure 9

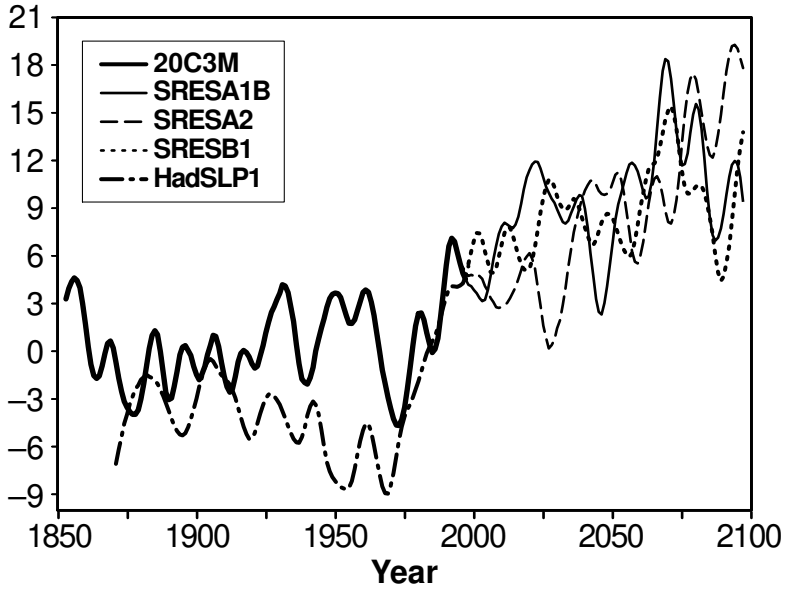
20C3M
SRESA1B
SRESA2
SRESB1
HadSLP1
21
18
15
12
9
6
3
0
–3
–6
–9
1850
1900
1950
2000
2050
2100
Year

Figure 10

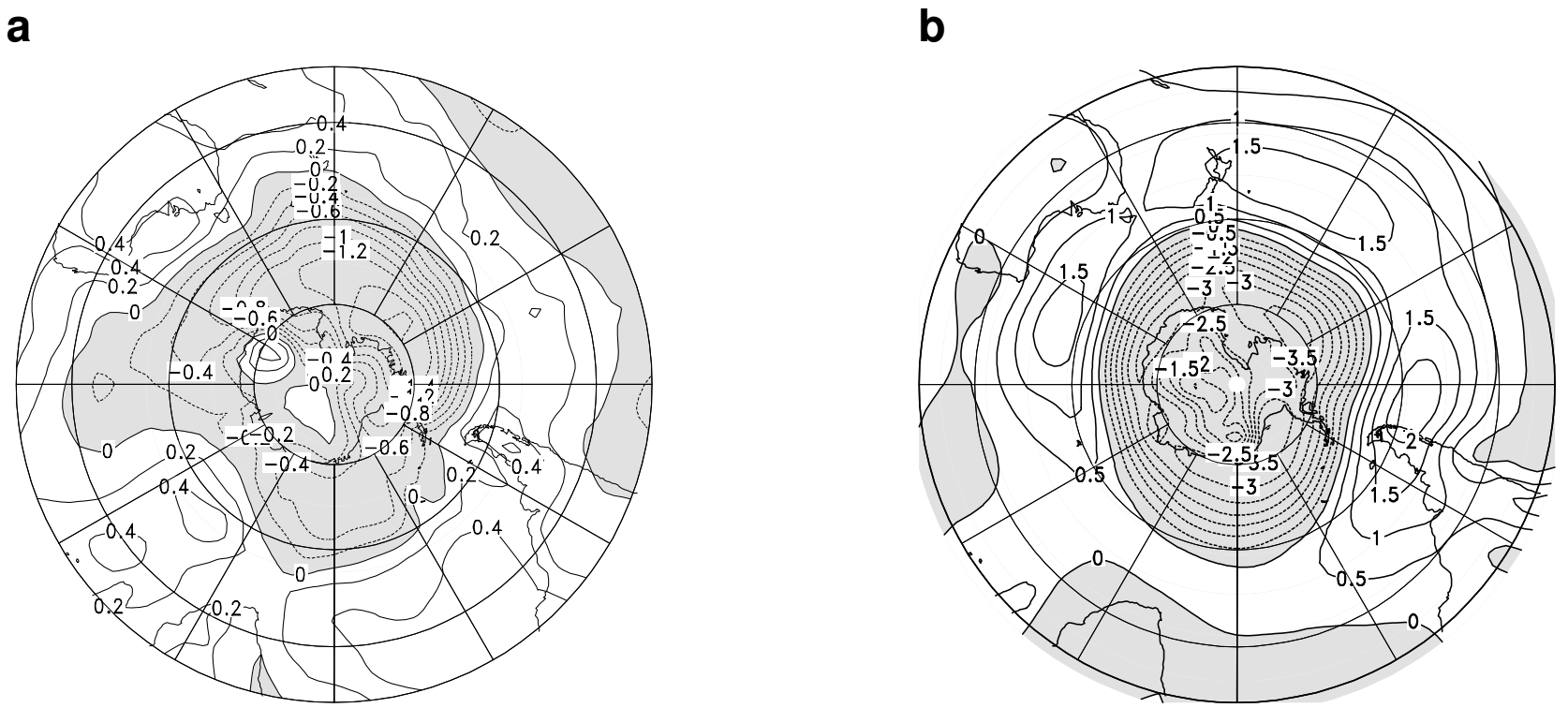

Figure 11

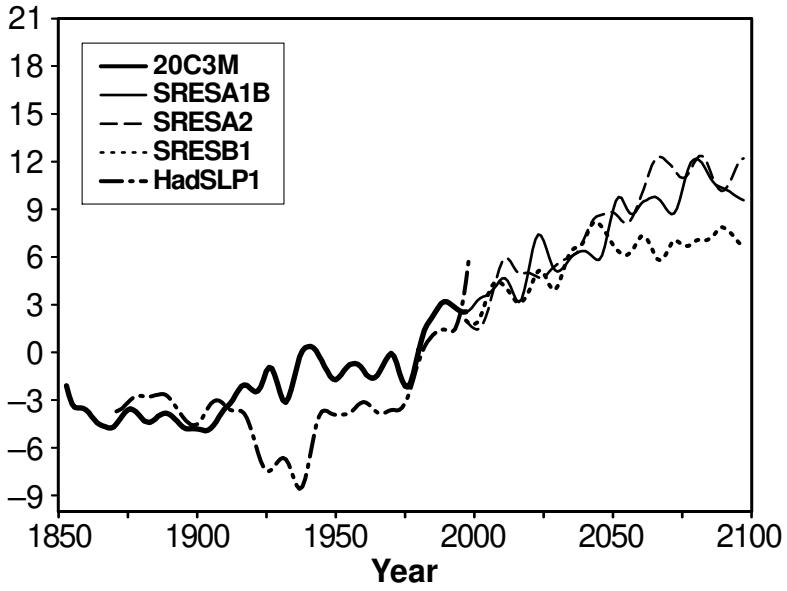
20C3M
SRESA1B
SRESA2
SRESB1
HadSLP1
21
18
15
12
9
6
3
0
−3
−6
−9
1850
1900
1950
2000
2050
2100
Year

Figure 12

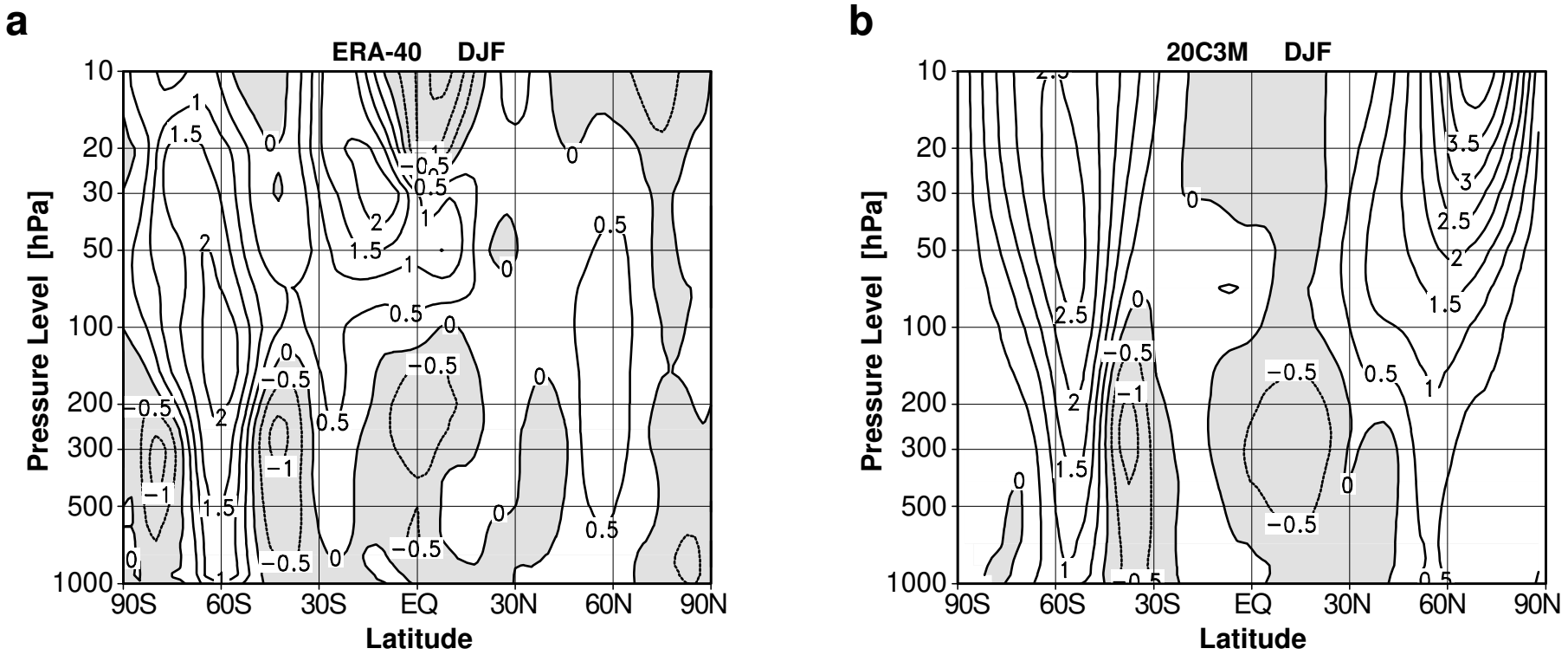
a
ERA-40 DJF
Pressure Level [hPa]
10
20
30
50
100
200
300
500
1000
90S
60S
30S
EQ
30N
60N
90N
Latitude
b
20C3M DJF
Pressure Level [hPa]
Latitude

Figure 13

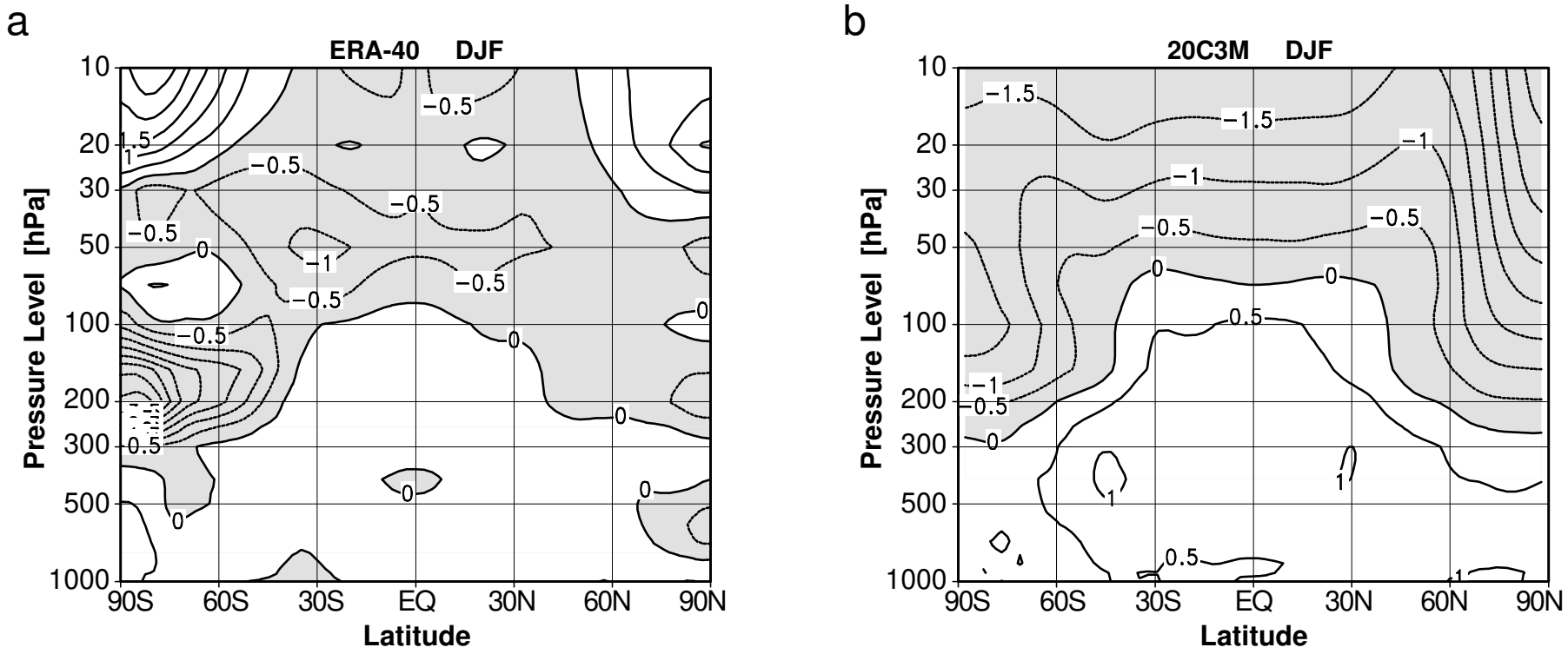
a
ERA-40 DJF
Pressure Level [hPa]
10
20
30
50
100
200
300
500
1000
90S
60S
30S
EQ
30N
60N
90N
Latitude
b
20C3M DJF
Pressure Level [hPa]
Latitude

Figure 14

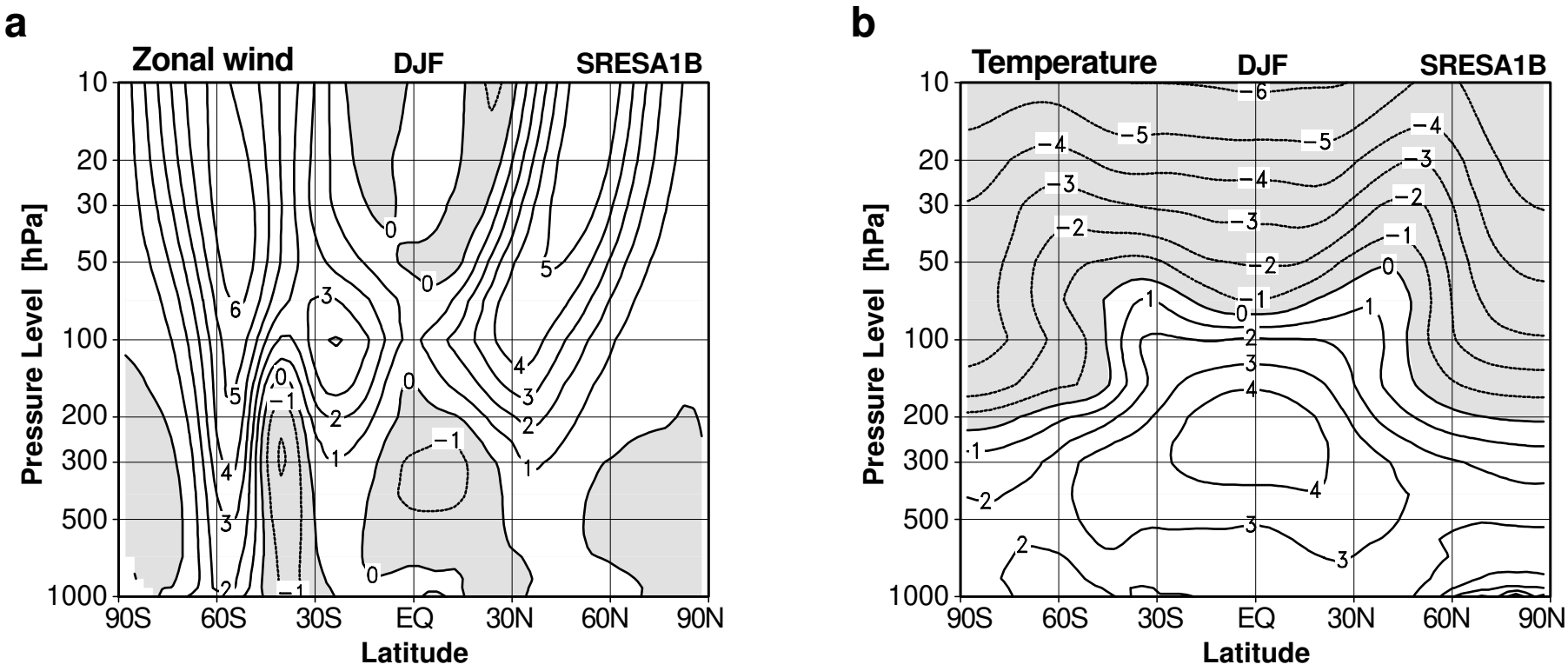
a
Zonal wind
DJF
SRESA1B
Pressure Level [hPa]
10
20
30
50
100
200
300
500
1000
90S
60S
30S
EQ
30N
60N
90N
Latitude
b
Temperature
DJF
SRESA1B
Pressure Level [hPa]
Latitude

Figure 15

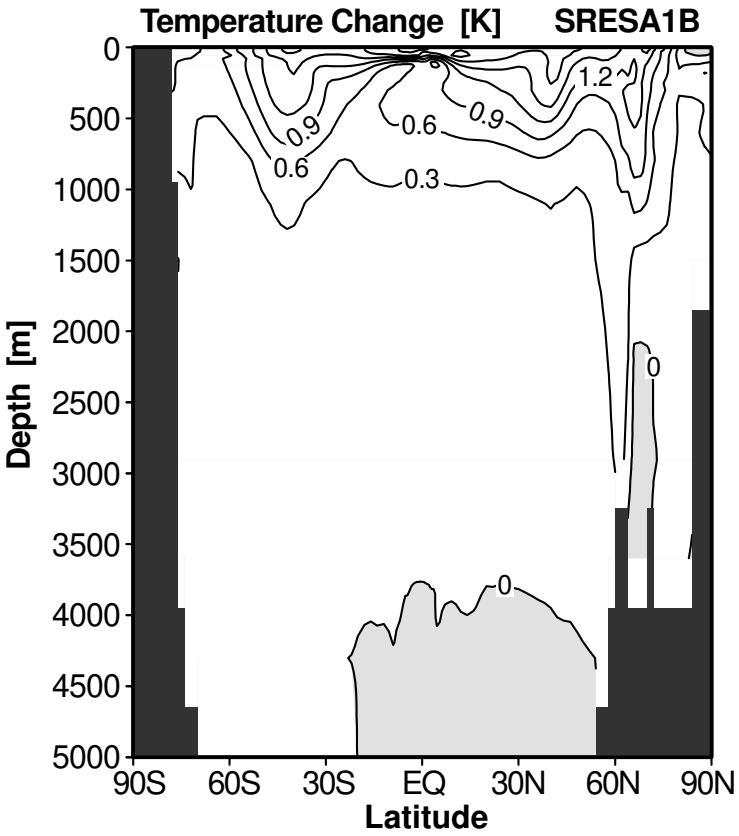
Temperature Change [K] SRESA1B
Depth [m]
0
500
1000
1500
2000
2500
3000
3500
4000
4500
5000
90S
60S
30S
EQ
30N
60N
90N
Latitude
1.2
0.9
0.6
0.3
0.9
0.6
0
0

Figure 16

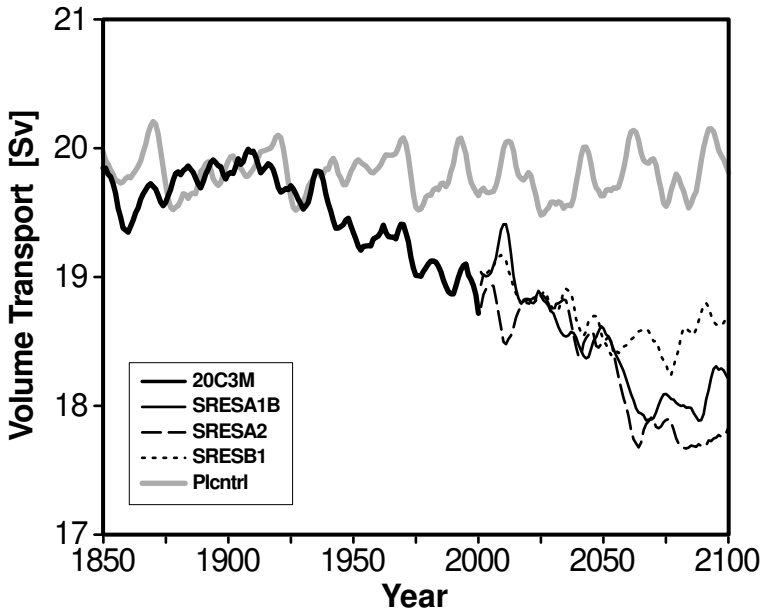
21
20
19
18
17
Volume Transport [Sv]
1850
1900
1950
2000
2050
2100
Year
20C3M
SRESA1B
SRESA2
SRESB1
Plcntrl

Figure 17

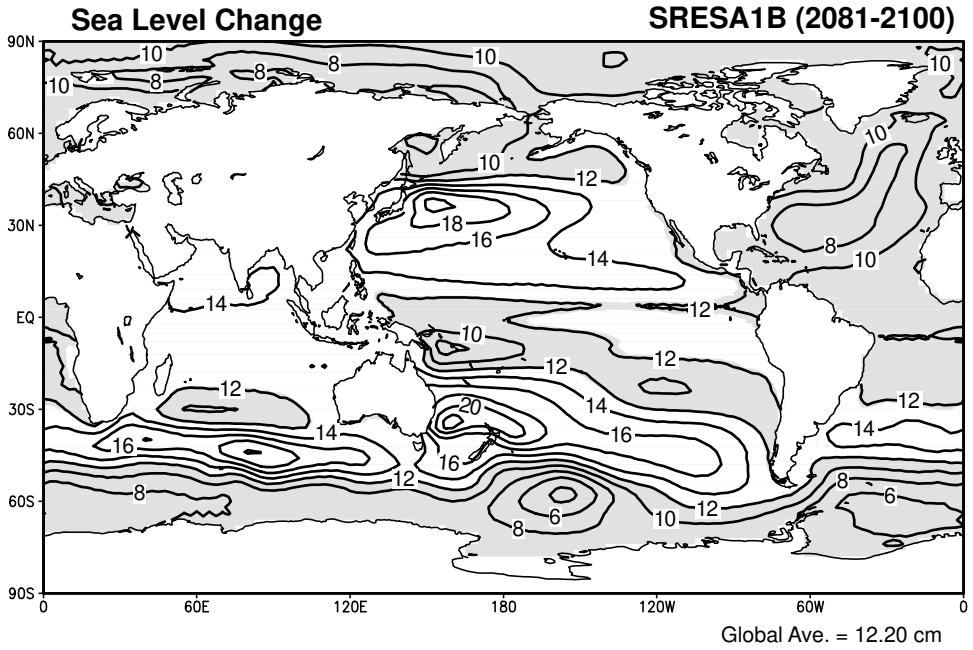
Sea Level Change
SRESA1B (2081-2100)
90N
60N
30N
EQ
30S
60S
90S
0
60E
120E
180
120W
60W
0
Global Ave. = 12.20 cm

Figure 18

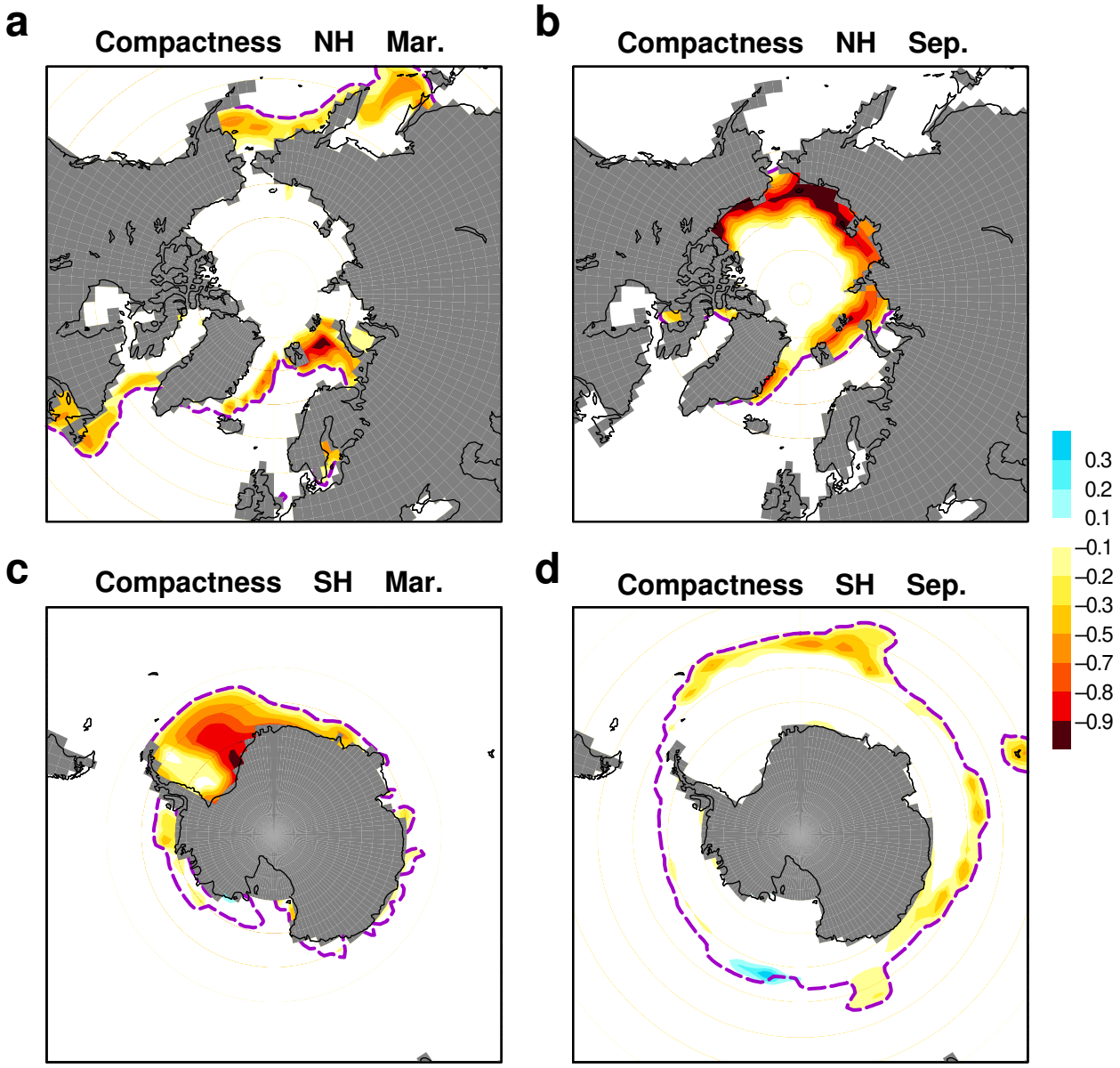
a
Compactness NH Mar.
b
Compactness NH Sep.
c
Compactness SH Mar.
d
Compactness SH Sep.
0.3
0.2
0.1
−0.1
−0.2
−0.3
−0.5
−0.7
−0.8
−0.9

Figure 19